submitted to *Geophys. J. Int.*

Automatic Bayesian polarity determination

D.J. Pugh[1,2,3*], R.S. White [1] and P.A.F. Christie[2]

[1]Bullard Laboratories, Department of Earth Sciences, University of Cambridge

[2]Schlumberger Gould Research, High Cross, Cambridge

[3]Now at McLaren Applied Technologies, McLaren Technology Centre, Chertsey Road, Woking

*Email:david.j.pugh@cantab.net

In original form 23rd September, 2015, in revised form 9th April, 2016.

SUMMARY

The polarity of the first motion of a seismic signal from an earthquake is an important constraint in earthquake source inversion. Microseismic events often have low signal-to-noise ratios, which may lead to difficulties estimating the correct first-motion polarities of the arrivals. This paper describes a probabilistic approach to polarity picking that can be both automated and combined with manual picking. This approach includes a quantitative estimate of the uncertainty of the polarity, improving calculation of the polarity probability density function for source inversion. It is sufficiently fast to be incorporated into an automatic processing workflow. When used in source inversion, the results are consistent with those from manual observations. In some cases, they produce a clearer constraint on the range of high-probability source mechanims, and are better constrained than source mechanisms determined using a uniform probability of an incorrect polarity pick.

Keywords: *Earthquake source observations, Computational seismology, Statistical seismology, Earthquake ground motions, Probability distributions, Numerical solutions*

1 INTRODUCTION

First-motion-based source inversion of earthquakes can be used to constrain nodal planes and to help estimate the source parameters. The use of first-motion polarities was proposed by Nakano (1923) and first implemented by Byerly (1926). These first-motion polarities of the phase arrivals provide an important constraint on the focal mechanism.

There are several source inversion approaches that utilise first-motion polarities to determine the source type, such as FPFIT (Reasenberg & Oppenheimer 1985), which uses P-polarities to determine the double-couple source, HASH (Hardebeck & Shearer 2002, 2003), which can also incorporate amplitude ratios in determining the double-couple source, and FOCMEC (Snoke 2003), which uses P, SH and SV polarities and amplitude ratios to search for double-couple sources. These inversion approaches are often limited (as in these three cases) to a double-couple source model.

Manual polarity picking is time consuming, especially for large microseismic data sets with large numbers of receivers and low signal-to-noise ratios. Modern workflows often process the data automatically, so the addition of a slow manual step into the automated workflow is undesirable.

The first motion of a seismic signal can often be hard to discern from background noise and filter artefacts, especially for low-magnitude events. Consequently, a robust first-motion source inversion requires some understanding of the likelihood of an incorrect polarity measurement. While the human eye and judgement are often correct when manually picking the polarity of an arrival on a seismic trace, it is usually recorded simply as being either positive or negative, although additional information in the pick such as whether it is impulsive or emergent, as well as the pick weight, can be used as indicators of the polarity pick quality. Determination of the first motion using a binary classification does not allow the assignment of any quantitative value to reflect the level of measurement uncertainty. Many automatic approaches which can be used to determine polarities usually produce results with a binary classification (Baer & Kradolfer 1987; Aldersons 2004; Nakamura 2004).

One common approach to deal with errors in the polarity picks is to allow a certain number of mistaken polarities in a fault plane solution (Reasenberg & Oppenheimer 1985); another is to provide a probability of a mistaken pick (Hardebeck & Shearer 2002, 2003). Nevertheless, these approaches do not account for how likely it is that

an interpreter picks an arrival incorrectly, because this depends on both the noise on the particular trace and the arrival characteristics, such as whether the arrival onset is impulsive or emergent. Consequently, the probability of an incorrect pick differs for each arrival.

The approach described in this paper eschews this binary classification for the polarity observations. Instead the probability of an arrival being a positive or negative polarity is calculated from the waveform. This allows the inclusion of uncertainty in the arrival in a quantitative assessment of the polarity, and can be incorporated in the earthquake source inversion approach of Pugh et al. (2016).

2 BAYESIAN POLARITY PROBABILITY DETERMINATION

It is possible to determine the polarity of any given waveform at any point; doing this to the whole waveform retains the polarity information, while discarding both amplitude and phase information. Consequently, determining the arrival polarity is reduced to selecting which time, t, is representative of the correct arrival pick.

A basic approach used for manual determination of polarities can be broken down into two steps:

1. Look for the next amplitude maximum or minimum after the arrival-onset time t in the waveform.

2. Determine the polarity from the type of stationary value, with positive polarity corresponding to an amplitude maximum and negative to a minimum).

Such an approach is straightforward computationally. The polarity can be described at a given time t by a function, $\mathrm{pol}\,(\mathrm{t})$, which takes values switching between -1 and
Figure 1 1, for the next maximum or minimum.

Arrival-time picks are often imprecise with respect to the first motion of the arrival because of noise effects. Furthermore, when using automated pickers, the choice of picking approach often leads to a later triggering compared to manually refined picks (Fig. 1). However, manually refined picks can be affected by personal preferences, leading to different manual arrival-time picks on the arrival phase by different people. For an uncertain arrival-time pick, the identification of positive or negative polarity may not be meaningful, as it may not refer to the true first arrival. Therefore, this issue can be overcome by estimating the probability of the first motion being positive or negative.

The amplitude change of the peak of the candidate first arrival can provide an indication of the likelihood that it has been affected by noise. Therefore, the amplitude change could be used to give the arrival some quality weighting. However, it may be more precise to consider how likely the polarity is to be positive based on the measured noise level, i.e., by determining the probability that the amplitude change of the candidate first arrival is not due to the noise.

2.1 Polarity Probability Function

The probability density function (PDF) of a given signed amplitude A having polarity $Y = y$, where $y = \pm 1$, at an instrument is given by a step function such as the Heaviside step function $\mathrm{H}(x) = \int_{-\infty}^{x} \delta(s)\mathrm{d}s$, defined in terms of the delta function $\delta(x)$. This PDF is dependent on the amplitude measurement error, ϵ, which arises both from the background noise and the measurement error in the device. The measured amplitude is given by the sum of the true amplitude and the measurement error, so, the PDF for observing a given amplitude value is dependent on both the true amplitude and the measurement error, and is:

$$\mathrm{p}\left(Y = y \,|\, A, \epsilon\right) = \mathrm{H}\left(y\left(A + \epsilon\right)\right). \tag{1}$$

Marginalisation (e.g. Sivia 2000) includes the measurement error in the probability. It is assumed that only the mean and the variance of the noise are measurable and, therefore, the most ambiguous distribution (maximum entropy) is the Gaussian distribution, as can be shown using variational calculus (Pugh et al. 2016). This choice of distribution is valid independent of the actual random noise distribution. However, any correlated non-random noise should be accounted for. If more statistics of the noise are known, such as the higher order moments, the appropriate maximum entropy distribution should be used.

For data that have been de-meaned (DC-offset corrected) over a suitable window, the noise can be assumed to have zero mean, and a standard deviation σ_{mes} independent of the amplitude, so that the probability that the ϵ is the current amplitude error is Gaussian:

$$\mathrm{p}\left(\epsilon|\sigma_{\mathrm{mes}}\right) = \frac{1}{\sqrt{2\pi\sigma_{\mathrm{mes}}^2}} \mathrm{e}^{-\frac{\epsilon^2}{2\sigma_{\mathrm{mes}}^2}}. \tag{2}$$

Marginalising over ϵ gives:

$$\mathrm{p}\left(Y=y\,|\,A,\sigma_{\mathrm{mes}}\right) = \int_{-\infty}^{\infty}\mathrm{p}\left(Y=y\,|\,A,\epsilon\right)\mathrm{p}\left(\epsilon|\sigma_{\mathrm{mes}}\right)\mathrm{d}\epsilon, \tag{3}$$

$$\mathrm{p}\left(Y=y\,|\,A,\sigma_{\mathrm{mes}}\right) = \int_{-\infty}^{\infty}\mathrm{H}\left(y\left(A+\epsilon\right)\right)\frac{1}{\sqrt{2\pi\sigma_{\mathrm{mes}}^2}}\mathrm{e}^{-\frac{\epsilon^2}{2\sigma_{\mathrm{mes}}^2}}\mathrm{d}\epsilon. \tag{4}$$

The product $y\epsilon$ in Eq. 1 changes the sign of the noise to reflect the polarity, but because the PDF for ϵ is symmetric, this change in sign has no effect. The integral can be simplified using a behaviour of the step function:

$$\int_{-\infty}^{\infty}\mathrm{H}\left(x+\epsilon\right)f\left(\epsilon\right)\mathrm{d}\epsilon = \int_{-x}^{\infty}f\left(\epsilon\right)\mathrm{d}\epsilon, \tag{5}$$

which gives:

$$\mathrm{p}\left(Y=y\,|\,A,\sigma_{\mathrm{mes}}\right) = \int_{-yA}^{\infty}\frac{1}{\sqrt{2\pi\sigma_{\mathrm{mes}}^2}}\mathrm{e}^{-\frac{\epsilon^2}{2\sigma_{\mathrm{mes}}^2}}\mathrm{d}\epsilon. \tag{6}$$

This can be rewritten, using the symmetry of the normal distribution about the mean, as:

$$\mathrm{p}\left(Y=y\,|\,A,\sigma_{\mathrm{mes}}\right) = \int_{-\infty}^{yA}\frac{1}{\sqrt{2\pi\sigma_{\mathrm{mes}}^2}}\mathrm{e}^{-\frac{\epsilon^2}{2\sigma_{\mathrm{mes}}^2}}\mathrm{d}\epsilon = \frac{1}{2}\left(1+\mathrm{erf}\left(\frac{yA}{\sqrt{2}\sigma_{\mathrm{mes}}}\right)\right). \tag{7}$$

It is important to note that the behaviour of this PDF produces a higher probability for stations with larger amplitudes, as these stations are more likely to have arrival polarities that are not perturbed by noise. However, if the noise standard deviation (σ_{mes}) is low, the PDF approaches the step function, reducing this effect.

Since polarity observations are either positive or negative, because the nodal region of a moment tensor source is infinitesimally thin, the probability for both cases should sum to unity.

2.2 Arrival Polarity Probability

Section 2.1 has given the PDF for observing a polarity given some amplitude and noise level. However, there is an additional time dependence when estimating the polarity of an arrival. For an arrival, the PDF for a positive polarity, $Y = +1$, depends on the amplitude at a given time. The amplitude can be written in terms of the polarity function, $\mathrm{pol}\left(\mathrm{t}\right)$, and the absolute amplitude change between stationary values, $\Delta\left(t\right)$,

and noise standard deviation, σ_{mes}, giving:

$$\mathrm{p}\left(Y = + \,|\, t, \sigma_{\text{mes}}\right) = \frac{1}{2}\left(1 + \mathrm{erf}\left(\frac{\mathrm{pol\,(t).}\Delta\left(t\right)}{2\sigma_{\text{mes}}}\right)\right), \tag{8}$$

where the standard deviation from Eq. 7 has been multiplied by $\sqrt{2}$ to account for using the amplitude change between maximum and minimum, rather than the noise amplitude as described in Section 2.1. This PDF has been marginalised (Sivia 2000, Section 1.3) with respect to the measurement noise, but retains dependence on the noise standard deviation (σ_{mes}). However, it is also necessary to marginalise for the arrival-time error to account for this uncertainty in the arrival time. This uncertainty depends on the arrival, but could be based on the perceived quality of the pick on some scale such as the common 0-4 scale (best - worst) from HYPO71 (Lee & Lahr 1975).

A possible, although perhaps arbitrary, probability distribution for pick accuracy is a Gaussian distribution around the pick. However, the method described below is independent of the form of distribution chosen. For a Gaussian distribution around the pick, the probability that the arrival time is actually at t for a given arrival-time pick (τ) with standard deviation (σ_τ) is:

$$\mathrm{p}\left(t \,|\, \tau, \sigma_\tau\right) = \frac{1}{\sqrt{2\pi{\sigma_\tau}^2}}\,\mathrm{e}^{-\frac{(t-\tau)^2}{2\sigma_\tau^2}}. \tag{9}$$

The arrival-time standard deviation is related to the arrival-time uncertainty, and can be set either as a mapping from the pick quality or from an arrival detection PDF, as discussed in Section 3.

The PDF for the polarity of an arrival is, therefore, given by the product of the polarity probabilities (Eq. 8), and the time probabilities (Eq. 9):

$$\mathrm{p}\left(Y = + \,|\, t, \tau, \sigma_{\text{mes}}, \sigma_\tau\right) = \frac{1}{2}\left(1 + \mathrm{erf}\left(\frac{\mathrm{pol\,(t).}\Delta\left(t\right)}{2\sigma_{\text{mes}}}\right)\right)\mathrm{p}\left(t \,|\, \tau, \sigma_\tau\right), \tag{10}$$

$$\mathrm{p}\left(Y = - \,|\, t, \tau, \sigma_{\text{mes}}, \sigma_\tau\right) = \frac{1}{2}\left(1 + \mathrm{erf}\left(\frac{-\mathrm{pol\,(t).}\Delta\left(t\right)}{2\sigma_{\text{mes}}}\right)\right)\mathrm{p}\left(t \,|\, \tau, \sigma_\tau\right). \tag{11}$$

If a Gaussian arrival-time PDF (Eq. 9) is used, the PDFs from Eqs 10 and 11 are given

by:

$$\mathrm{p}\left(Y=+\,|\,t,\tau,\sigma_{\mathrm{mes}},\sigma_\tau\right) = \frac{1}{2}\left(1+\mathrm{erf}\left(\frac{\mathrm{pol\,(t).\Delta\,}(t)}{2\sigma_{\mathrm{mes}}}\right)\right)\frac{1}{\sqrt{2\pi{\sigma_\tau}^2}}\,\mathrm{e}^{-\frac{(t-\tau)^2}{2\sigma_\tau^2}}, \quad (12)$$

$$\mathrm{p}\left(Y=-\,|\,t,\tau,\sigma_{\mathrm{mes}},\sigma_\tau\right) = \frac{1}{2}\left(1+\mathrm{erf}\left(\frac{-\mathrm{pol\,(t).\Delta\,}(t)}{2\sigma_{\mathrm{mes}}}\right)\right)\frac{1}{\sqrt{2\pi{\sigma_\tau}^2}}\,\mathrm{e}^{-\frac{(t-\tau)^2}{2\sigma_\tau^2}}. \quad (13)$$

These PDFs are still time dependent, but this can be marginalised by integrating over all possible arrival times. In most cases, it is sufficient to take large limits (t_{min} and t_{max}) compared to the width of the arrival-time PDF , where the arrival-time PDF is approximately zero:

$$\mathrm{p}\left(Y=+|\tau,\sigma_{\mathrm{mes}},\sigma_\tau\right) = \int_{t_{min}}^{t_{max}}\frac{1}{2}\left(1+\mathrm{erf}\left(\frac{\mathrm{pol\,(t).\Delta\,}(t)}{2\sigma_{\mathrm{mes}}}\right)\right).\frac{1}{\sqrt{2\pi{\sigma_\tau}^2}}\,\mathrm{e}^{-\frac{(t-\tau)^2}{2\sigma_\tau^2}}\,\mathrm{d}t. \quad (14)$$

In the case of a Gaussian arrival-time PDF, suitable limits are $\tau \pm 10\sigma_\tau$. which have probabilities that are approximately zero$\left(\sim 10^{-23}\right)$. Similar marginalisation of the PDF from Eq. 13 gives the probability of a negative arrival, $\mathrm{p}\left(Y=-|\tau,\sigma_{\mathrm{mes}},\sigma_\tau\right)$.

The probabilities calculated by marginalising with respect to time are normalised provided the arrival-time PDF (Eq. 9) is normalised. This is clear because the anti-symmetry of the error function, erf, means that the sum of the amplitude probabilities is time independent and sums to unity:

$$\mathrm{p}\left(Y=+|\tau,\sigma_{\mathrm{mes}},\sigma_\tau\right)+\mathrm{p}\left(Y=-|\tau,\sigma_{\mathrm{mes}},\sigma_\tau\right) = \int_{t_{min}}^{t_{max}}\mathrm{p}\left(t\,|\,\tau,\sigma_\tau\right)\mathrm{d}t, \quad (15)$$

$$\mathrm{p}\left(Y=+|\tau,\sigma_{\mathrm{mes}},\sigma_\tau\right)+\mathrm{p}\left(Y=-|\tau,\sigma_{\mathrm{mes}},\sigma_\tau\right) \approx 1. \quad (16)$$

Figure 2

When the uncertainty, σ_τ, in the Gaussian arrival-time PDF (Eq. 9) increases, more stationary points on the waveform have non-zero arrival-time probabilities, and the arrival-time PDF is flattened. This can be seen in Fig. 2, which shows that for a synthetic arrival, when the arrival-time uncertainty and noise level are increased, the probabilities

Figure 3 tend towards 0.5.

Fig. 3 shows the different steps for evaluating the polarity probabilities for an example synthetic arrival with white noise. The calculated probabilities for the pick are: $\mathrm{p}\left(Y=+|\tau,\sigma_{\mathrm{mes}},\sigma_\tau\right)=0.33$, and $\mathrm{p}\left(Y=-|\tau,\sigma_{\mathrm{mes}},\sigma_\tau\right)=0.67$.

The approach described in this paper is not intended to produce a first motion estimate in the former binary classification, but instead to leave the results as probabilities directly. Nevertheless, it is possible to map the probabilities to the binary polarities, as

may be desirable for event classification. In this case, some significance level should be chosen for assigning the polarity values,

$$Y = \begin{cases} +1 & \mathrm{p}\left(Y = +|\tau, \sigma_{\mathrm{mes}}, \sigma_\tau\right) \geqslant q \\ 0 & q > \mathrm{p}\left(Y = +|\tau, \sigma_{\mathrm{mes}}, \sigma_\tau\right) > 1 - q \\ -1 & \mathrm{p}\left(Y = +|\tau, \sigma_{\mathrm{mes}}, \sigma_\tau\right) \leqslant 1 - q \end{cases}, \tag{17}$$

where q is a manually chosen probability value which reflects the desired confidence in the polarity direction estimation. In this case the values between q and $1-q$ have been assigned a polarity of 0, corresponding to no reported measurement, rather than zero polarity. Alternatively, the probabilities could be represented graphically as shown in Section 4, allowing for easy comparison between different events.

2.3 Choosing the Arrival Time PDF

This approach is independent of the choice of time PDF. When using automated picking, the PDF can be chosen based on both the automated picker used and any observed shifting produced in a manual review of the picks (Section 3). The arrival-time PDF should have significant probability over the onset of the arrival, rather than the whole arrival, as this can lead to large numbers of stationary points with significant arrival time probabilities, leading to an uncertain polarity probability estimate.

Fig. 1 shows a histogram of P and S arrival time shifts for the coalesence microseismic mapping (CMM) autopicker (Drew et al. 2005, 2013) for all pick weights. The mean shift is non-zero, likely due to poor-quality picks that are improved manually and the CMM tendency to pick on the peak rather than the onset. Therefore, the choice of a Gaussian probability around the CMM pick is not a poor one, although the mean could be chosen to be a small time shift (δt) before the automatic pick, to compensate for the CMM tendency to pick slightly late:

$$\mathrm{p}\left(t \,|\, \tau, \sigma_\tau\right) = \frac{1}{\sqrt{2\pi {\sigma_\tau}^2}} \, \mathrm{e}^{-\frac{(t-\tau+\delta t)^2}{2\sigma_\tau^2}}. \tag{18}$$

The arrival time PDF must be arrival specific, so as to reflect the confidence in the individual arrival time estimate, although the shape could be derived from an empirical distribution of arrival times for a subset of events in a data-set, such as that in Fig. 1,

with the width scaled by some measure of the arrival time uncertainty. Alternatively, as discussed below, the arrival time PDF can be based on some characteristic function of the data, perhaps as used in an automated picker (e.g. STA/LTA).

2.4 Manual and Automated Picking

Figure 4

This probabilistic approach produces an estimate of the likelihood of the polarity which can be combined with manual picking by using the manual observations as a prior probability for the automated measurements. The choice of prior probability for the polarity can have a large effect (Fig. 4). If the manual prior is large, the effect of the polarity probabilities is negligible, although as it is reduced to the null prior ($p_{\text{prior}} = 0.5$), the effect become more significant.

The prior has a strong effect, dominating the probabilities even for the incorrect polarity direction, but there is a clear difference in Fig. 4 between the correct (negative) and incorrect (positive) prior directions, with a much sharper trend towards a value of 1 for the incorrect prior direction. Consequently, even if the prior probability is large and in the incorrect direction, the resultant polarity probability for the correct direction will be larger than the corresponding prior probability value, and the probability is corrected towards the true value.

3 INTEGRATION WITH AUTOMATED MONITORING

The fast calculation speed allows this polarity estimation to be integrated into an automated processing workflow. This polarity information, in conjunction with other measurements such as amplitude ratios, can produce an estimate of the event source, allowing for better data quality control from observations and helping to flag interesting events in near real time. The accuracy of such an approach strongly depends on the accuracy of the arrival-time pick. As the error is increased, the polarity probabilities will tend towards 0.5 (Fig. 2). Therefore, provided the automated time picking is accurate, the polarity probabilities produced should show good consistency and, although manual refinement could still improve the result, the results from Eq. 14 should improve the

Figure 5

source constraints.

The arrival-time PDF can be based on some characteristic function from the chosen automated picking method. The CMM event detection algorithm (Drew et al. 2013)

uses a short-term averaging/long-term averaging (STA/LTA) detection function, which could be used as the arrival-time PDF in Eqs 10 and 11. In CMM, the detection function is fitted with a Gaussian approximation to produce an uncertainty estimate. However, Fig. 5 shows that using the STA/LTA function (Drew et al. 2013, eq. 1) or its Gaussian approximation often produces wide arrival time PDFs, encompassing most of the arrival rather than just the first motion. Furthermore, this detection function peaks away from the onset and leads to increased uncertainty in the pick time and, therefore, poorly defined polarity probabilities. Both the Gaussian approximation and the plain STA/LTA function show similar performance, providing little constraint on the polarity. Nevertheless, the maximum probability (Fig. 5 (d)) is in the negative direction, which is consistent with the arrival (Fig. 5 (a)).

Baer & Kradolfer (1987) introduced the concept of 'phase detectors' and 'phase pickers'. Phase detectors are relatively imprecise, and will be improved by human repicking. However, phase pickers should produce results that are comparable to those picked manually. Therefore, it may be better to use a phase picker to determine the onset and construct the arrival-time PDF more accurately. There are many approaches to accurate onset pickers such as the methods discussed by Baer & Kradolfer (1987): STA/LTA pickers (Allen 1978, 1982; Trnkoczy 2011); auto-regressive pickers (Takanami & Kitagawa; Takanami & Kitagawa; Nakamura); stationary analysis pickers (Nakamula et al. 2007); kurtosis based pickers (Ross & Ben-Zion 2014; Hibert et al. 2014); right to left pick averaging (RPA/LPA) (Zahradník et al. 2014), as well as many others. Withers et al. (1998) provide an overview of several of these different approaches, as do Di Stefano et al. (2006). Several of the STA/LTA-based approaches are shown in Fig. 6. Determining the parameters for these automated pickers is not always straightforward, and parameters must often be adjusted based on the general signal characteristics (Trnkoczy 2011; Zahradník et al. 2014). Figure 6

Many of these approaches produce characteristic functions that have a sharp increase at the onset (Ross & Ben-Zion 2014, fig. 3). So a possible definition of the arrival-time PDF could be a Gaussian using the size and onset of the peak in the characteristic function (F_{C}) as an indicator of the uncertainty, e.g,

$$\sigma_\tau = \frac{\tau_{\max} - \tau_{\min}}{F_{\mathrm{C}}\left(t = \tau_{\max}\right) - F_C\left(t = \tau_{\min}\right)}, \tag{19}$$

where $\tau_{\max}$ is the time of the maximum in the peak, and $\tau_{\min}$ is the time of the minimum. Fig. 6(b) shows an example of this arrival-time PDF for a recursive STA/LTA pick, which is more focussed on the first arrival, rather than the whole of the arrival phase. Fig. 6 shows that neither the CMM STA/LTA nor the RPA/LPA approaches is as good at resolving the arrival as the recursive STA/LTA method.

4 EXAMPLES

In the following examples, manual arrival time picks were made on both the synthetic and real data. The arrival noise levels were measured in a time window from half way between the start of the trace and the P-arrival. The exact window was constructed based on the P arrival time uncertainty so as to remove any significant probability of any signal occurring in the noise window. The noise estimate is important in Eq. 14, but since the stationary points used in this approach are by definition at the extrema of the values, the result from Eq. 7 is often close to 1 or 0 (Fig. 3 (b)), so errors in the noise estimate have less effect than errors in the arrival time uncertainty estimate.

4.1 Polarity PDF Plot

Figure 7

To present both the manual polarity picks and the polarity probability requires a new type of plot. Fig. 7 shows one approach. The positive polarity probabilities are represented as bars above the axis, and the negative below. Darker shading indicates better manual arrival time pick quality. The solid bars correspond to manual polarity picks, and cross-hatched bars correspond to directions without a manually picked polarity. This allows an easy comparison between the manual polarity picks and the results from this approach.

4.2 Synthetic Examples

Figure 8

The behaviour of the method for different noise levels and arrival-time picks was tested using synthetic arrivals generated by finite-difference modelling (Bernth & Chapman 2011). Fig. 8 shows the effects of varying the arrival-time pick on a trace with random Gaussian noise added to give an amplitude signal-to-noise ratio (SNR) of 10. The arrival-time uncertainty was left at the initial value ($\sigma_\tau = 0.01\text{s} = 1$ sample), meaning that even small variations in the trace could cause large changes in the estimated probability. For

this example, the probability of a negative arrival varied between 0.39 and 0.79, with the low probability values not consistent with the observed negative polarity of the arrival without noise. However, the inconsistent probabilities occur due to the arrival time picks being close to the positive part of the arrival, and later than the true pick. This indicates the importance of accurate arrival-time picks and good characterisation of the arrival-time PDFs, either as a Gaussian approximation around the arrival-time pick or using a detection function.

Figure 9

The background noise levels for a given pick time were varied using two different noise models: Gaussian and boxcar (Fig. 9). These show that the accuracy is good for low noise levels, but as the noise level approaches that of the signal, the noise can have very large effects on the observed waveform and polarity. There is a small dependence on the noise model, with mainly lower probabilities estimated from the positive polarity for the synthetic arrivals with boxcar noise. However, the values are still consistent with those from the Gaussian noise model, suggesting that the Gaussian noise is not a bad approximation. In practice the traces with low SNR (Figs 9(d), (e), and (f)) would probably be considered difficult to pick and, therefore, be assigned a larger time pick error.

These examples also demonstrate why an arrival-time PDF with some shift (Eq. 18) may be better, as the arrival-time picks in Figs 8 and 9 are closer to the onset rather than the first peak. Accordingly, the first motions are more likely to be after the pick time rather than equally likely before and after.

As shown in these examples, the approach is robust and can provide a qualitative value on the probability of the polarity being up or down, but the probabilities are inherently dependent on the accuracy of the arrival-time pick and the trace noise levels. Traces with a high SNR should produce a reliable result, but as the time pick uncertainty increases, the polarity probability tends to 0.5 (Fig. 2).

Figure 10

Fig. 10 shows that the automated approach usually agrees with the manually observed polarities, especially in the low-noise cases. However, as the noise levels increase, the solutions occasionally disagree with the manually observed polarities, although this is expected in the low-SNR examples.

Figure 11

This approach can also be used when evaluating S-phase polarities, even though these require rotation into the correct ray orientation to measure them. Consequently,

they cannot easily be determined without an estimate of the hypocentre, unlike the P-wave polarities. Fig. 11 shows an example of SH-wave measurements from a synthetic event with an amplitude SNR of 5. The SH polarities were manually picked on the transverse component after the location was determined by rotating into the vertical, radial and transverse (ZRT) components. The noise levels were again estimated by windowing before the arrival. For these observations, any increased signal due to the P-arrival should be considered as noise when estimating the SH-polarity probability, so the window was taken to include the P arrival time. The polarity probabilities show good consistency with the manually picked polarities.

4.3 Real Data

Table 1
Figure 12

Table 1 shows a comparison between the automated and manual polarity picks for one event from a July 2007 swarm beneath Mount Upptyppingar in Iceland (White et al. 2011), with the polarity PDF plot shown in Fig. 12. The manual observations and automatically determined solutions are consistent with good-quality arrival-time picks producing probabilities larger than 0.7 and often larger than 0.9. The poor picks

Figure 13

with large time uncertainties show that the resulting probabilities tend to 0.5 each, as

Figure 14

discussed in Section 2. Fig. 13 shows an example polarity PDF for one of the stations.

The results of the automated polarity picking for several events from the Krafla region of Iceland are shown in Fig. 14. For the most part, the automated polarity probabilities agree with the manual polarities; although there a few cases that disagree; these are usually caused by an error in the manual arrival-time pick. This error made the arrival-time PDF a poor approximation, often due to early or late picks being assigned a high pick quality, leading to narrow arrival-time PDFs before or after the first arrival. The strong agreement of the observations suggests that this approach works well with

Figure 15

real data and not just with synthetically generated events.

Fig. 15 shows the results from testing the polarity probability estimation with added noise levels on two traces from the Upptyppingar and Krafla data shown above. The results are consistent with those shown in Fig. 2, although there is a faster decay to the

Figure 16

0.5 probability line, and a wider spread of results, due to the more complex signal. Figs 16 and 17 show the effects of varying the time pick and noise level on the real data, and

Figure 17

again the results are consistent with those shown in Figs 8 and 9.

5 SOURCE INVERSION

The Bayesian approach proposed by Pugh et al. (2016) can easily be extended to include the automated polarity observations. The PDF for the observed polarity at a given time is dependent on the theoretical amplitude (A), the measurement uncertainty ($\epsilon\left(t\right)$), and the observed amplitude change ($\Delta\left(t\right) \geqslant 0$) (c.f. Eq. 1):

$$\mathrm{p}\left(\mathrm{pol\,(t)}|A, \Delta\left(t\right), \epsilon\left(t\right), t\right) = \mathrm{H}\left(\mathrm{pol\,(t)}\left(A + \frac{\epsilon\left(t\right)}{\Delta\left(t\right)}\left|A\right|\right)\right). \tag{20}$$

The theoretical amplitude depends on the source model.

Given that the standard deviation of the background noise (σ) can be estimated, the simplest noise model for the uncertainty, $\epsilon\left(t\right)$, on $\Delta\left(t\right)$ is a Gaussian distribution, with standard deviation $\sqrt{2}\sigma$ due to $\Delta\left(t\right)$ corresponding to the amplitude change. Marginalising with respect to the uncertainty gives (c.f. Eq. 4):

$$\mathrm{p}\left(Y\left(t\right) = \mathrm{pol\,(t)}|A, \Delta\left(t\right), \sigma, t\right) = \int_{-\infty}^{\infty} \frac{\mathrm{H}\left(\mathrm{pol\,(t)}\left(A + \frac{\epsilon(t)}{\Delta(t)}\left|A\right|\right)\right)}{\sqrt{2\pi\sigma^2}} \mathrm{e}^{-\frac{\epsilon(t)^2}{2\sigma^2}} \mathrm{d}\epsilon\left(t\right). \tag{21}$$

Following Appendix 2.1, the PDF is:

$$\mathrm{p}\left(Y\left(t\right) = \mathrm{pol\,(t)}|A, \Delta\left(t\right), \sigma, t\right) \quad = \quad \frac{1}{2}\left(1 + \mathrm{erf}\left(\frac{\mathrm{pol\,(t)}\Delta\left(t\right)\mathrm{sgn}\left(A\right)}{2\sigma}\right)\right). \tag{22}$$

This is not marginalised with respect to time, but there is a simplification that can be made here. The signum function in the PDF is equivalent to writing the PDF using the Heaviside step function $\mathrm{H}\left(x\right)$:

$$\begin{aligned}\mathrm{p}\left(Y\left(t\right) = \mathrm{pol\,(t)}|A, \Delta\left(t\right), \sigma, t\right) = \mathrm{H}\left(A\right)\frac{1}{2}\left(1 + \mathrm{erf}\left(\frac{\mathrm{pol\,(t)}\Delta\left(t\right)}{2\sigma}\right)\right) + \\ H\left(-A_i\right)\frac{1}{2}\left(1 + \mathrm{erf}\left(\frac{-\mathrm{pol\,(t)}\Delta\left(t\right)}{2\sigma}\right)\right).\end{aligned} \tag{23}$$

This form makes it easy to marginalise with respect to time because the modelled amplitude is independent of the time, so the time-marginalised PDF for source inversion is:

$$\mathrm{p}\left(\psi|A, \sigma, \tau, \sigma_\tau\right) = \mathrm{H}\left(A\right)\psi + \mathrm{H}\left(-A\right)\left(1 - \psi\right), \tag{24}$$

where ψ is the time-marginalised positive polarity PDF for the arrival (Eq. 14).

As with the manually determined polarity PDF from Pugh et al. (2016), it is possible that there could be a receiver orientation error with probability ϖ, leading to a flipped polarity, so Eq. 24 can be extended to:

$$\mathrm{p}\left(\psi|A,\sigma,\tau,\sigma_\tau,\varpi\right) = 1-\varpi+\left(2\varpi-1\right)\left[\mathrm{H}\left(A\right)+\psi-2\mathrm{H}\left(A\right)\psi\right]. \tag{25}$$

This is the polarity probabilities likelihood, which is included in the Bayesian source inversion by substituting into the source likelihood (Pugh et al. 2016, eqs 17 and 18) to give (using the same nomenclature as Table 2 from Pugh et al. (2016)):

$$\mathrm{p}\left(\mathbf{d}'\mid\mathbf{M},\tau,\mathbf{k}\right) = \iint\sum_{j=1}^{M}\prod_{i=1}^{N}\left[\mathrm{p}\left(\psi_i\mid\mathbf{A}_i=\mathbf{a}_{i;j}\cdot\tilde{\mathbf{M}},\sigma_i,\varpi_i,\tau_i,\sigma_{\tau_\mathrm{i}}\right)\mathrm{p}\left(\mathbf{R}_i\mid\mathbf{A}_i=\mathbf{a}_{i;j}\cdot\tilde{\mathbf{M}},\sigma_i,\tau_i\right)\right]$$
$$\mathrm{p}\left(\sigma\right)\mathrm{p}\left(\varpi\right)\mathrm{d}\sigma\mathrm{d}\varpi, \tag{26}$$

for the source likelihood including location uncertainty, and:

$$\mathrm{p}\left(\mathbf{d}'\mid\mathbf{M},\tau,\mathbf{k}\right) = \iint\sum_{k=1}^{Q}\sum_{j=1}^{M}\prod_{i=1}^{N}\left[\mathrm{p}\left(\psi_i\mid\mathbf{A}_i=\mathbf{a}_{i;jk}\cdot\tilde{\mathbf{M}},\sigma_i,\varpi_i,\tau_i,\sigma_{\tau_\mathrm{i}}\right)\mathrm{p}\left(\mathbf{R}_i\mid\mathbf{A}_i=\mathbf{a}_{i;jk}\cdot\tilde{\mathbf{M}},\sigma_i,\tau_i\right)\right]$$
$$\mathrm{p}\left(\sigma\right)\mathrm{p}\left(\varpi\right)\mathrm{d}\sigma\mathrm{d}\varpi, \tag{27}$$

for the source likelihood including location and velocity model uncertainty. These PDFs (Eqs 26 and 27) have observed data,$\mathbf{d}'$ consisting of polarity probabilities, ψ, and amplitude ratios $\mathbf{R}$, and known parameters, $\mathbf{k}$, consisting of the arrival time errors σ_τ, and the ray paths, $\mathbf{a}_{i;j}$ for receiver i and location position j, calculated from the station locations and velocity model, with $\mathbf{a}_{i;jk}$ corresponding to the ray paths for receiver i, source location j and velocity model k. The PDFs are evaluated for the moment tensor, $\mathbf{M}$, with six vector, $\tilde{\mathbf{M}}$, with theoretical amplitudes $\mathbf{A}_i$given by the inner product of the receiver ray paths and the moment tensor six-vector.

Care must be taken with the data independence. Manual polarity observations must only be used in the source inversion in combination with automated polarity observations as a prior, otherwise the resulting source PDF will be artificially sharpened.

This quantitative method for including noise in the polarity determination is unlike

the more qualitative approaches for manual polarity observations such as those described by Brillinger et al. (1980), Walsh et al. (2009) and Pugh et al. (2016).

5.1 Examples

Figure 18

The source inversion results for a synthetic double-couple event and a real event from the Upptyppingar dyke swarm in 2007 (White et al. 2011) were evaluated using the Bayesian approach of Pugh et al. (2016), adapted for automated results (Eqs 26 and 27). The results for the full moment tensor inversion are plotted on a lune plot (Tape & Tape 2012). Fig. 18 shows the positions of the different source types on the plot.

Figure 19

The results for the source inversion using automated picking resemble those of the manual picking (Figs 19-22), but there is usually a wider range of possible solutions because most of the proposed solutions have at least a small non-zero probability. In some cases, the solution can be improved by additional constraint from receivers with no manual polarity pick, but a suitable arrival time pick. This is shown by the example from the Upptyppingar dyke swarm, which has a few receivers without manual polarity picks but with suitable arrival-time picks to estimate the polarity probabilities. The double-couple solutions from the automated polarity inversion tend to have a clearer demarcation between the high-probability solutions and the lower-probability solutions, as can be seen in Figs 19 and 20.

Figure 20

A common approach to dealing with polarity uncertaintys is to allow a blanket probability of a pick being incorrect (p_{mispick}) (Hardebeck & Shearer 2002, 2003). This is equivalent to setting the value of ψ in Eq. 25 to either $1-p_{\mathrm{mispick}}$ or p_{mispick} depending on whether the manual pick is positive or negative. Unlike the automated polarity approach, including this arbitrary blanket probability of a mistaken pick cannot account for the most-difficult-to-pick arrivals being most likely to be incorrect. Consequently, the range of solutions is often not overly broad. The double-couple solutions from the automated polarities in Fig. 20 show a stronger demarcation between the low- and high-probability solutions than those using a blanket probability of a mistaken pick, although the ranges are similar. The full moment tensor solutions in Fig. 20 have very similar distributions for both of the inversions, with a less peaked range of solutions than the ordinary manual polarity solutions from the same event shown in Fig. 19.

Figure 21

Although the choice of time PDF is independent of the approach, the CMM STA/LTA

(Fig. 5) was tested as a possible PDF. Fig. 21 shows that this time PDF can work in low-noise environments, but in a higher-noise environment it may not be possible to determine a solution. This is clear in the solutions for the Upptyppingar event, which has no constraint on the possible source for both the double-couple and full moment tensor inversions because the variations in probability are too low. The low-noise synthetic example shows good agreement with the east-west plane, but the north-south plane has a much larger range of high probability solutions. However, the approach may provide some constraint on the source PDF in the high-noise case if there are enough receivers sampling the focal-sphere. Using an arrival-time PDF from a well calibrated onset picker
Figure 22 (Section 3) would provide a much larger improvement in the source constraints.

Using manual polarity picks as a prior probability further sharpens the source PDF, leading to a sharper solution than even the manual polarities (Fig. 22). The full moment tensor solutions are also constrained better by the prior, compared to the equivalent solutions in Fig. 19.

6 SUMMARY AND DISCUSSION

The Bayesian approach to automated polarity determination proposed in this paper is a quantitative approach that enables rigorous incorporation of measurement uncertainties into the polarity probability estimates. It is an alternative approach to the traditional binary classification of polarities, and can be adapted for use with any onset or arrival-time picking method, either manual or automatic. The polarity probabilities estimated using this method provide a quantitative approach for including the polarity uncertainties in the source inversion. This contrasts with many common approaches, including the qualitative approach for manual polarity observation described by Brillinger et al. (1980), Walsh et al. (2009) and Pugh et al. (2016), and the arbitrarily determined probability of a mistaken pick (Hardebeck & Shearer 2002, 2003).

The polarity probabilities have a clear dependence on the time pick accuracy and the noise level of the trace, requiring an accurate arrival time pick. Poorly characterised arrival-time pick uncertainties lead to little discrimination in the polarity probabilities. Consequently, when an automated arrival picking approach is used, accurate onset picks with results comparable to picks made by a human are required, otherwise the resultant arrival-time PDF is usually too wide.

The choice of arrival-time PDF can be adjusted depending on the perceived quality of the arrival time picking approach. For an automated picker, the arrival-time PDF peak can be shifted to just before the pick if the automated pick tends to be late, as is the case for the CMM STA/LTA picker. The arrival-time PDF can also be adjusted using the pick quality estimate, such as the pick weight (0-4 range from HYPO71 (Lee & Lahr 1975)), although a range with finer discretisation would prove more accurate.

In the real-world cases from the Upptyppingar volcano and Krafla in Iceland, there are few differences between the results obtained from manual and automated picking. The estimation of the probability of correct first motions produces a quantitative estimate of the uncertainty of the polarities that carries through to the calculation of the resulting source mechanism PDF. In the cases where the automated and manual picks seem to disagree, this can be attributed partially to human error in the arrival time and manual polarity determinations.

The time required for calculating the PDFs is fast compared with that required for manual picking. This approach adds little time to an automated processing workflow, and can be included easily into near-real-time event detection, unlike the much slower manual polarity picking. Additionally, the approach is useful for determining polarities of phases measured on location-dependent seismogram components, such as the SH phase. These are often ignored in source inversion due to the requirement to return and pick the polarities after the event has been located.

ACKNOWLEDGEMENTS

This work was funded under a Natural Environment Research Council (NERC) studentship as a CASE award with Schlumberger. Seismometers were borrowed from the NERC SEIS-UK (loan 842), who also archive the data. We thank Mike Williams and Chris Chapman for their help and advice. We would also like to thank our two anonymous reviewers for helping improve this manuscript. Department of Earth Sciences, Cambridge contribution number ESC3601

References

Aldersons, F., 2004. *Toward a three-dimensional crustal structure of the Dead Sea region from local earthquake tomography*, Ph.D. thesis, Tel Aviv.

Allen, R. V., 1978. Automatic earthquake recognition and timing from single traces, *Bulletin of the Seismological Society of America*, **68**(5), 1521–1532.

Allen, R. V., 1982. Automatic phase pickers: their present use and future prospects, *Bulletin of the Seismological Society of America*, **72**(6B), S225–S242.

Baer, M. & Kradolfer, U., 1987. An automatic phase picker for local and teleseismic events, *Bulletin of the Seismological Society of America*, **77**(4), 1437–1445.

Bernth, H. & Chapman, C., 2011. A comparison of the dispersion relations for anisotropic elastodynamic finite-difference grids, *Geophysics*, **76**(3), WA43–WA50.

Beyreuther, M., Barsch, R., Krischer, L., Megies, T., Behr, Y., & Wassermann, J., 2010. ObsPy: a Python toolbox for seismology, *SRL: Electronic Seismologist*.

Brillinger, D. R., Udias, A., & Bolt, B. A., 1980. A probability model for regional focal mechanism solutions, *Bulletin of the Seismological Society of America*, **70**(1), 149–170.

Byerly, P., 1926. The Montana earthquake of June 28, 1925, G.M.C.T., *Bulletin of the Seismological Society of America*, **16**(4), 209–265.

Di Stefano, R., Aldersons, F., Kissling, E., Baccheschi, P., Chiarabba, C., & Giardini, D., 2006. Automatic seismic phase picking and consistent observation error assessment: application to the Italian seismicity, *Geophysical Journal International*, **165**(1), 121–134.

Drew, J., Leslie, D., Armstrong, P., & Michaud, G., 2005. Automated microseismic event detection and location by continuous spatial mapping, in *Society of Petroleum Engineers Annual Technical Conference and Exhibition*.

Drew, J., White, R. S., Tilmann, F., & Tarasewicz, J., 2013. Coalescence microseismic mapping, *Geophysical Journal International*, **195**(3), 1773–1785.

Hardebeck, J. L. & Shearer, P. M., 2002. A new method for determining first-motion focal mechanisms, *Bulletin of the Seismological Society of America*, **92**(6), 2264–2276.

Hardebeck, J. L. & Shearer, P. M., 2003. Using S / P amplitude ratios to constrain the focal mechanisms of small earthquakes, *Bulletin of the Seismological Society of America*, **93**(6), 2434–2444.

Hibert, C., Mangeney, A., Grandjean, G., Baillard, C., Rivet, D., Shapiro, N. M., Satriano, C., Maggi, A., Boissier, P., Ferrazzini, V., & Crawford, W., 2014. Automated identification, location, and volume estimation of rockfalls at Piton de la Fournaise volcano, *Journal of Geophysical Research: Earth Surface*, **119**, 1082–1105.

Knopoff, L. & Randall, M. J., 1970. The compensated linear-vector dipole: a possible mechanism for deep earthquakes, *Journal of Geophysical Research*, **75**(26), 4957–4963.

Lee, W. H. K. & Lahr, J. C., 1975. HYPO71 (Revised): A computer program for determining hypocenter, magnitude and first motion pattern of local earthquakes, Tech. Rep. 300, USGS.

Nakamula, S., Takeo, M., Okabe, Y., & Matsuura, M., 2007. Automatic seismic wave arrival detection and picking with stationary analysis: Application of the KM2O-Langevin equations, *Earth, Planets and Space*, **59**(6), 567–577.

Nakamura, M., 2004. Automatic determination of focal mechanism solutions using initial motion polarities of P and S waves, *Physics of the Earth and Planetary Interiors*, **146**(3-4), 531–549.

Nakano, H., 1923. Notes on the nature of the forces which give rise to the earthquake motions, *Seis- tool. Bull. Central Met. Obs. Japan*, **1**, 92–120.

Pugh, D. J., White, R. S., & Christie, P. A. F., 2016. A Bayesian method for microseismic source inversion, *Geophysical Journal International*, (submitted).

Reasenberg, P. A. & Oppenheimer, D., 1985. FPFIT, FPPLOT and FPPAGE: Fortran computer programs for calculating and displaying earthquake fault-plane solutions - OFR 85-739, Tech. rep., USGS.

Ross, Z. E. & Ben-Zion, Y., 2014. Automatic picking of direct P, S seismic phases and fault zone head waves, *Geophysical Journal International*, **199**(1), 368–381.

Shimizu, H., Ueki, S., & Koyama, J., 1987. A tensile-shear crack model for the mechanism of volcanic earthquakes, *Tectonophysics*, **144**, 287–300.

Sivia, D. S., 2000. *Data Analysis: A Bayesian Tutorial*, Oxford Univ Press.

Snoke, J. A., 2003. FOCMEC: FOCal MEChanism determinations, Tech. rep.

Takanami, T. & Kitagawa, G., 1988. A new efficient procedure for the estimation of onset times of seismic waves, *Journal of Physics of the Earth*, **36**, 267–290.

Takanami, T. & Kitagawa, G., 1991. Estimation of the arrival times of seismic waves

by multivariate time series model, *Annals of the Institute of Statistical mathematics*, **43**(3), 403–433.

Tape, W. & Tape, C., 2012. A geometric setting for moment tensors, *Geophysical Journal International*, **190**(1), 476–498.

Trnkoczy, A., 2011. Understanding and parameter setting of STA/LTA trigger algorithm: IS 8.1, *IASPEI New manual of seismological observatory practice*.

Walsh, D., Arnold, R., & Townend, J., 2009. A Bayesian approach to determining and parametrizing earthquake focal mechanisms, *Geophysical Journal International*, **176**(1), 235–255.

White, R. S., Drew, J., Martens, H. R., Key, J., Soosalu, H., & Jakobsdóttir, S. S., 2011. Dynamics of dyke intrusion in the mid-crust of Iceland, *Earth and Planetary Science Letters*, **304**(3-4), 300–312.

Withers, M., Aster, R., Young, C., Beiriger, J., Harris, M., Moore, S., & Trujillo, J., 1998. A comparison of select trigger algorithms for automated global seismic phase and event detection, *Bulletin of the Seismological Society of America*, **88**(1), 95–106.

Zahradník, J., Janský, J., & Plicka, V., 2014. Analysis of the source scanning algorithm with a new P-wave picker, *Journal of Seismology*, **19**(2), 423–441.

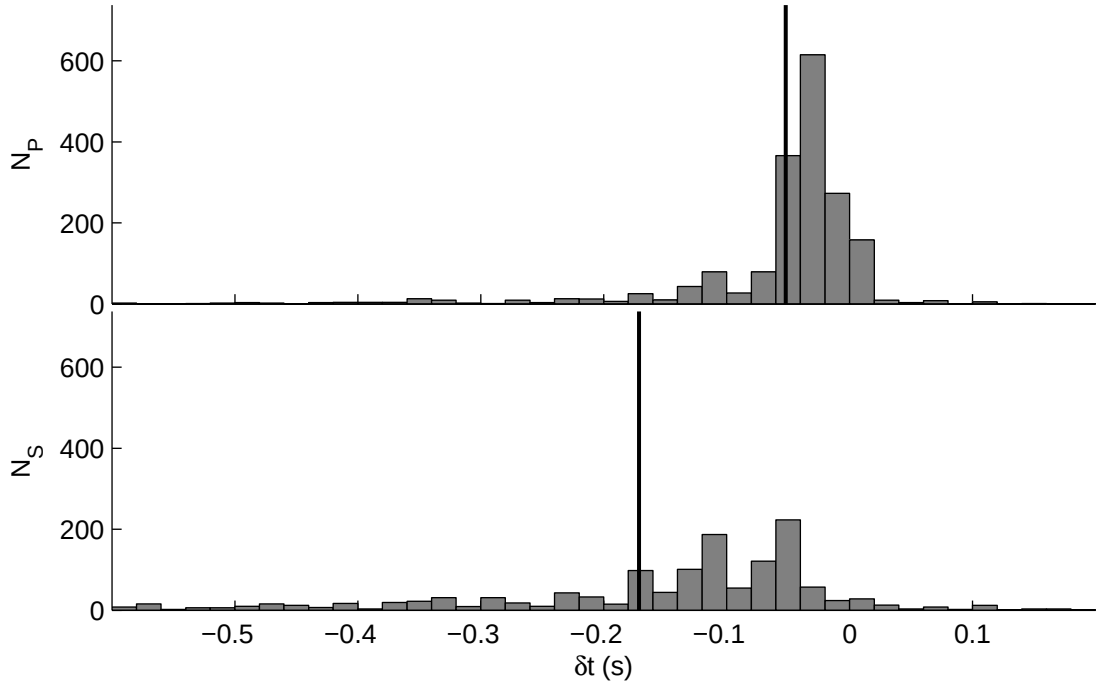

Figure 1. Histogram of 1791 arrival time pick differences between automatic and manually refined picks. The vertical black lines show the mean shift for each pick type. The top histogram is for P arrivals, and the bottom shows S arrivals. Typical frequency of the arrival is ~ 10 Hz. Automatic picks were made using the coalescence microseismic mapping method (Drew et al. 2013) on microseismic data from the Askja region of Iceland. The automatic picks were made using an STA window of 0.2 seconds and an LTA window of 1.0 seconds.

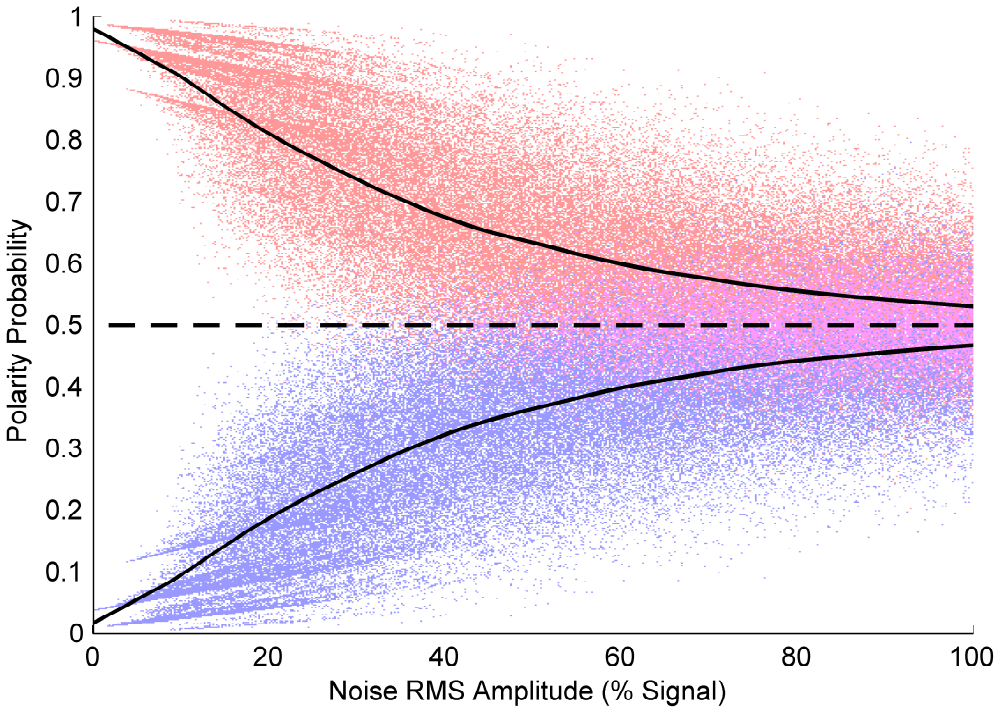

Figure 2. Distribution of the positive (red) and negative (blue) polarity probabilities for 100 000 samples of a simple synthetic trace with added random Gaussian noise. The original waveform had a positive polarity. The time pick was not changed, but the time uncertainty was increased as the noise level increased. The dashed line indicates a 50% probability of positive or negative arrival, corresponding to no net information, and the solid lines indicate a smoothed mean of the positive and negative polarity probabilities (e.g. Eq. 14).

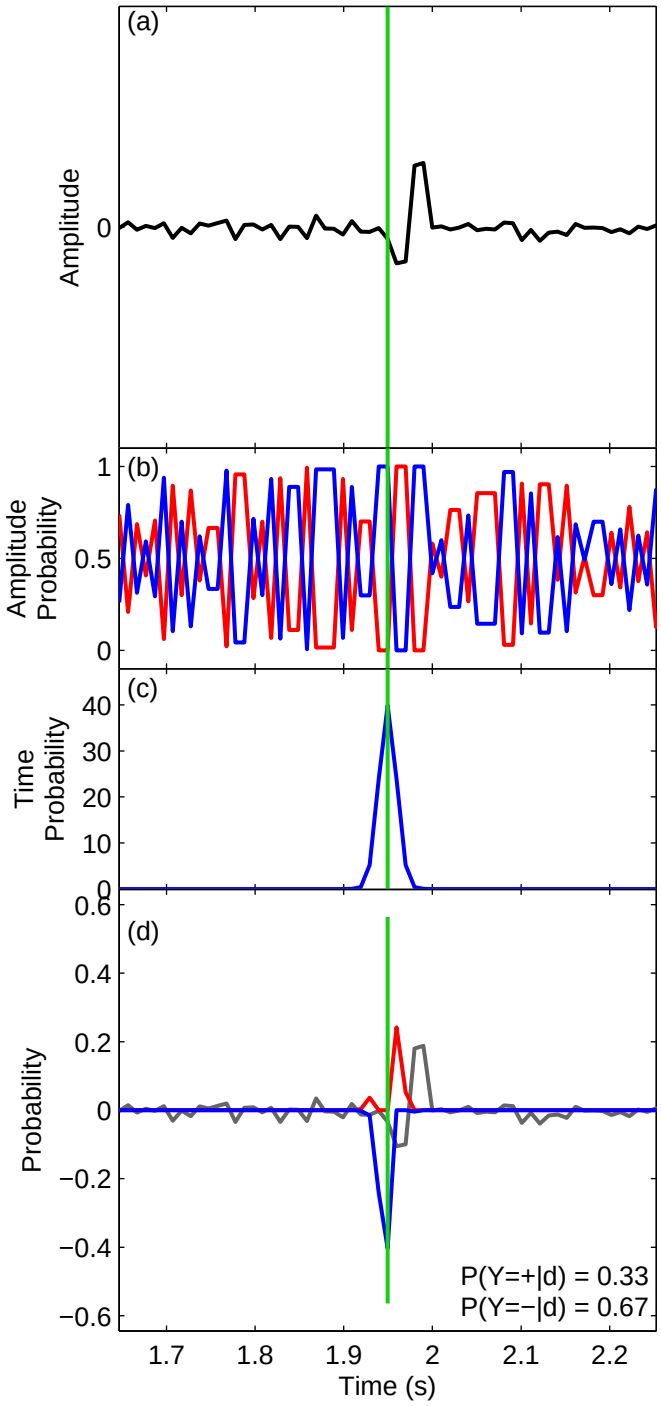

Figure 3. Plot of trace and the associated PDFs for the different stages of the probabilistic polarity determination. (a) shows the waveform; (b) shows the amplitude PDFs for positive (red) and negative (blue) polarities having accounted for noise, (c) shows the time probability function, and (d) shows the combined PDFs for positive (red) and negative (blue) polarities superimposed on the waveform (grey). The vertical lines correspond to the arrival-time pick.

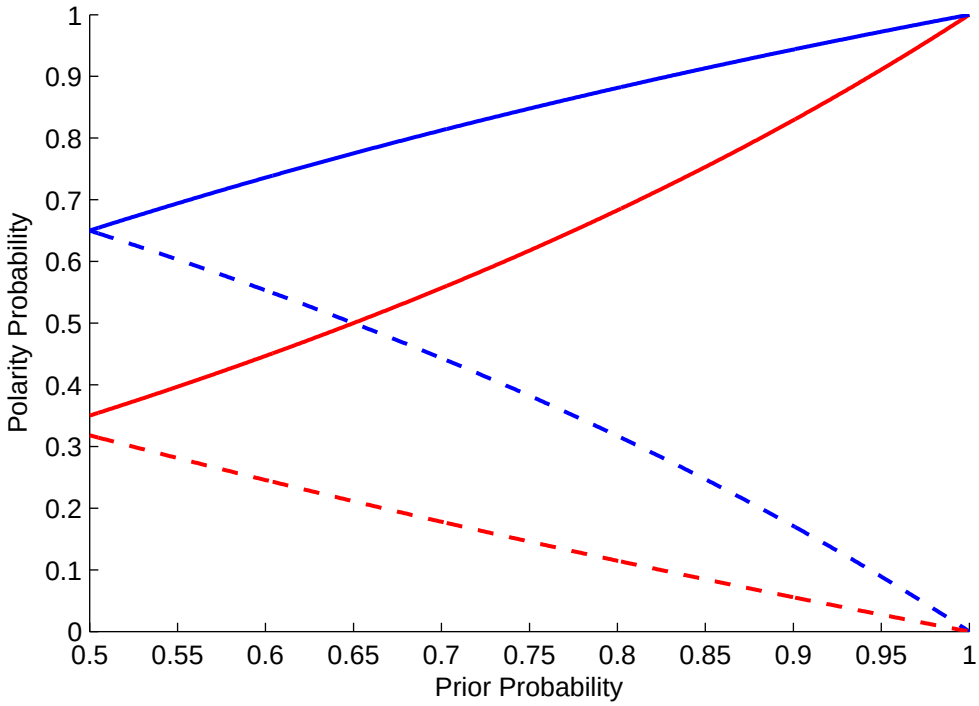

Figure 4. Polarity probabilities for the arrival from Fig. 3 for different manual prior probabilities. The red lines correspond to the positive polarity probability, and the blue to the negative polarity probability. The solid lines show the probabilities when the manual polarity pick is positive, and the dashed lines show the probabilities for a negative manual polarity pick.

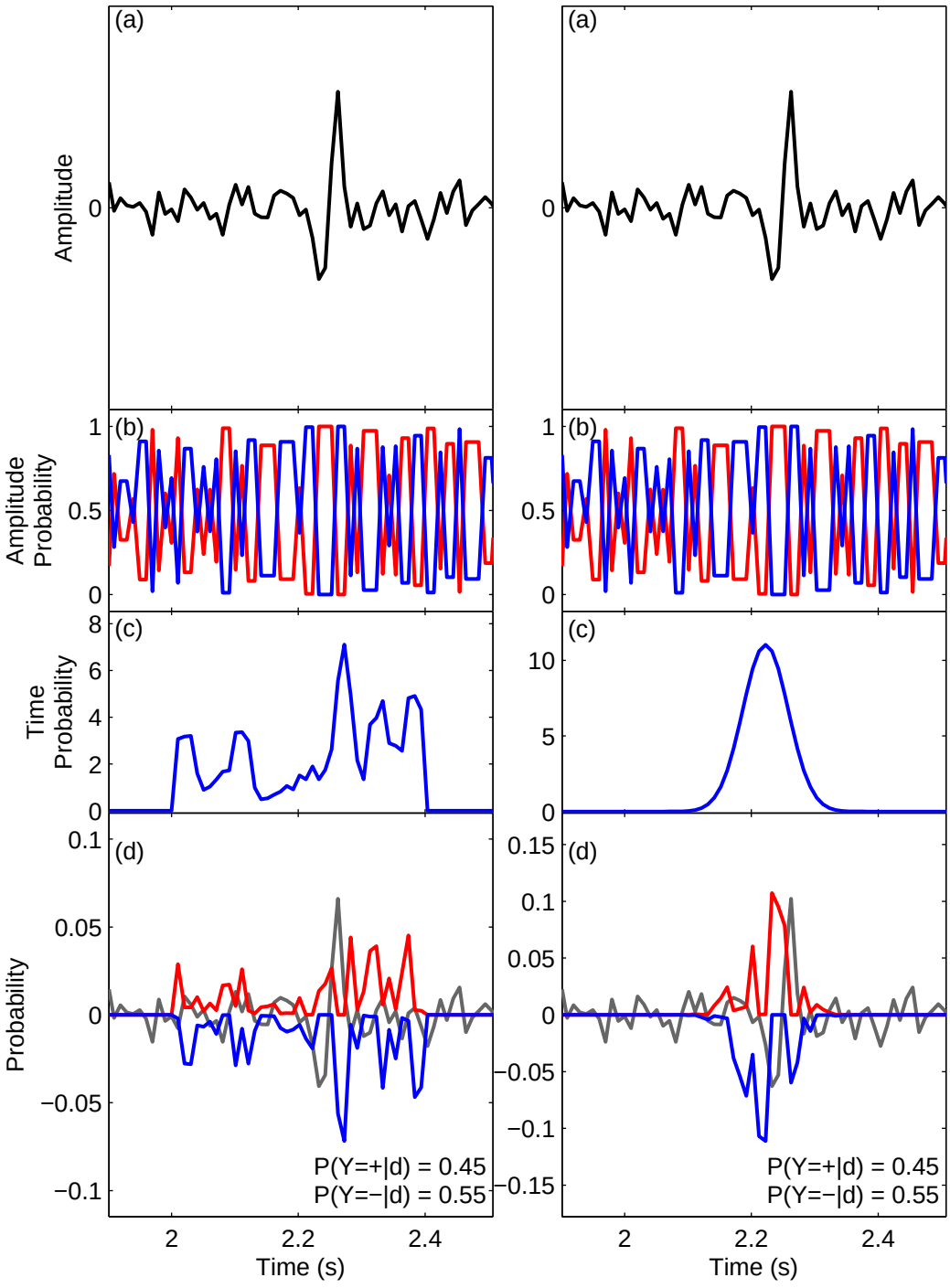

Figure 5. Plot of the trace and associated PDFs for the different stages, same type of plot as Fig. 3. The left column shows the STA/LTA detection function used as the arrival-time PDF, while the right shows the Gaussian approximation generated from Drew et al. (2013). The STA/LTA parameters chosen were based on those described by Drew et al. (2013, Section 2.1); here, the STA window size is one period of the signal.

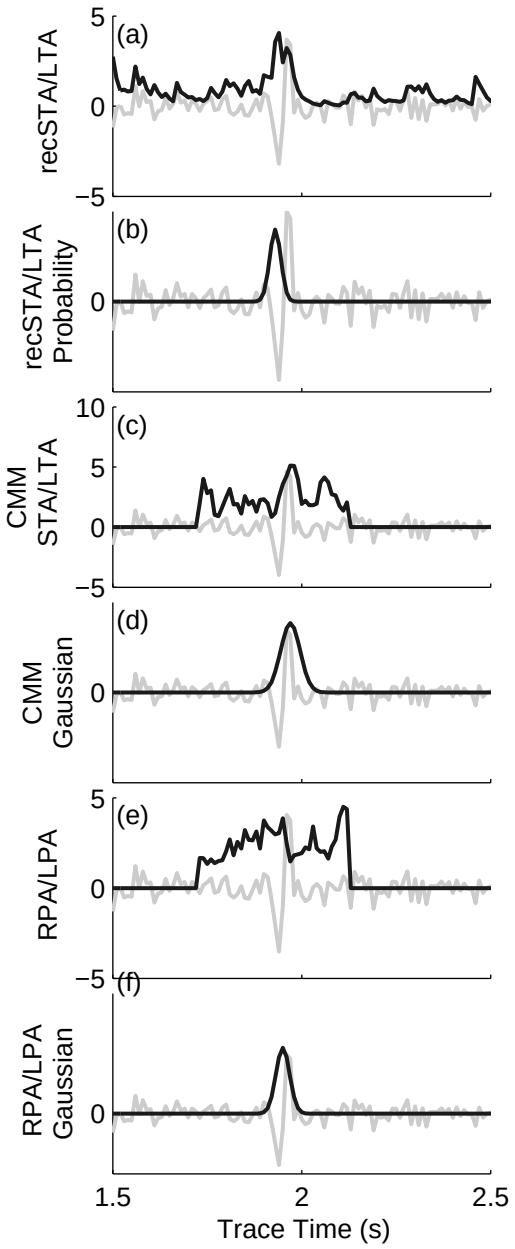

Figure 6. Example arrival-time PDF constructed from different STA/LTA trigger functions. The onset function is shown in black and the example P-wave arrival is shown in grey. (a) shows the recursive STA/LTA function from ObsPy (Beyreuther et al. 2010). (b) shows the arrival-time PDF given by Eq. 19 peaked in the middle of the onset. (c) and (d) show the truncated CMM STA/LTA detection function and the approximated Gaussian. (e) and (f) show the RPA/LPA approach of Zahradník et al. (2014) and the approximate Gaussian fit using the same approach as for the CMM STA/LTA function.

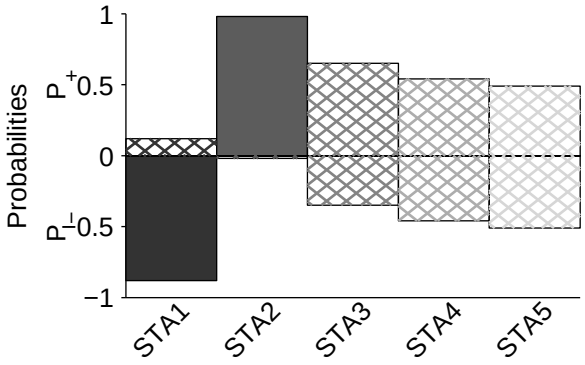

Figure 7. Example polarity PDF plot; the positive polarity probabilities are given by the length of the bar above the axis and the negative by the length of the bar below the axis. The darker the shading, the better the manual pick quality. The solid bars correspond to manual polarity pick directions, and cross-hatched bars correspond to positive or negative polarities with no manual polarity picks. The station names are given beneath the corresponding obervation, on the x-axis. STA1 has $\mathrm{p}\left(Y = -|\tau, \sigma_{\mathrm{mes}}, \sigma_\tau\right) = 0.87$ and a pick quality of 0 on the HYPO71 0-4 (best-worst) scale (Lee & Lahr 1975), along with a manually observed negative polarity. STA2 has $\mathrm{p}\left(Y = +|\tau, \sigma_{\mathrm{mes}}, \sigma_\tau\right) = 0.98$, a pick quality of 1, and a manually observed positive polarity. STA3 has a pick quality of 2 and no manually observed polarity. STA4 has a pick quality of 3 and, again, no manually observed polarity, while STA5 has a pick quality of 4 and no manually observed polarity.

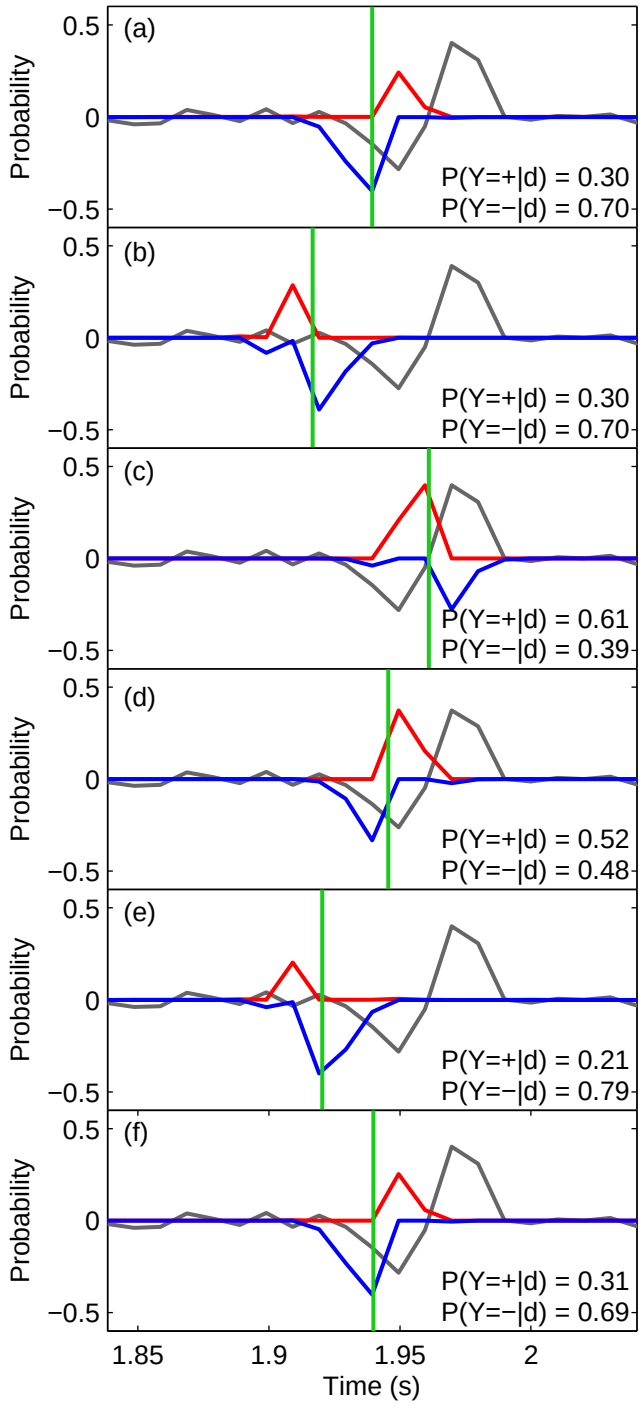

Figure 8. PDF plots for varying arrival-time picks on the same waveform.The original arrival-time pick is shown in (a), with randomly varied arrival-time picks in (b-f). The waveform is shown in grey, with the positive polarity PDF in red and the negative polarity PDF in blue. The vertical lines correspond to the arrival-time picks. The arrival-time picks were varied by adding a time shift randomly sampled from a Gaussian distribution.

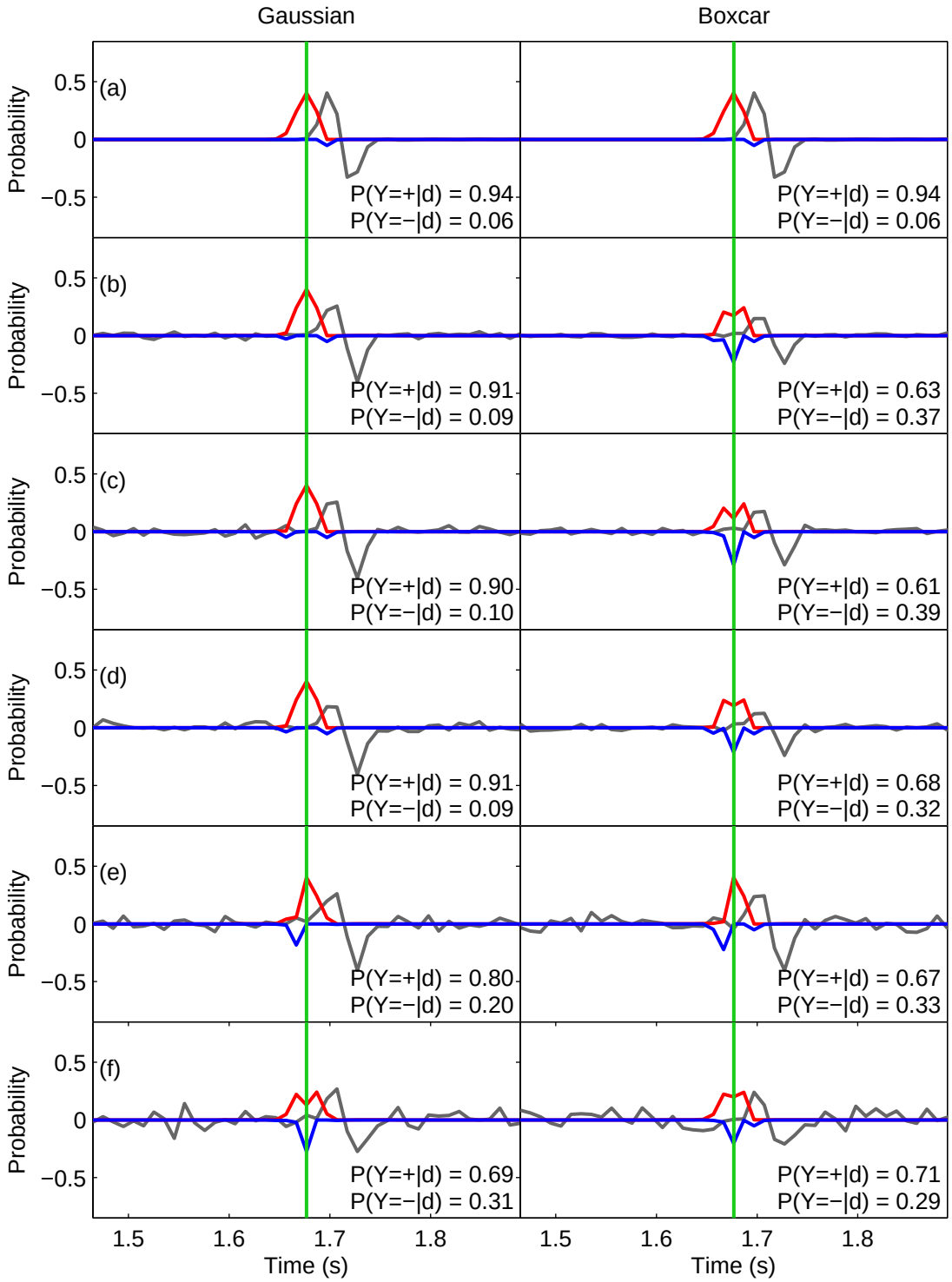

Figure 9. PDF plots for varying Gaussian and boxcar noise levels for the same waveform. The noise levels are: (a) No noise, (b) SNR=10, (c) SNR=5, (d) SNR=3, (e) SNR=2, and (f) SNR=1.2. The waveform is shown in grey, with the positive polarity PDF in red and the negative polarity PDF in blue. The vertical lines correspond to the arrival-time pick.

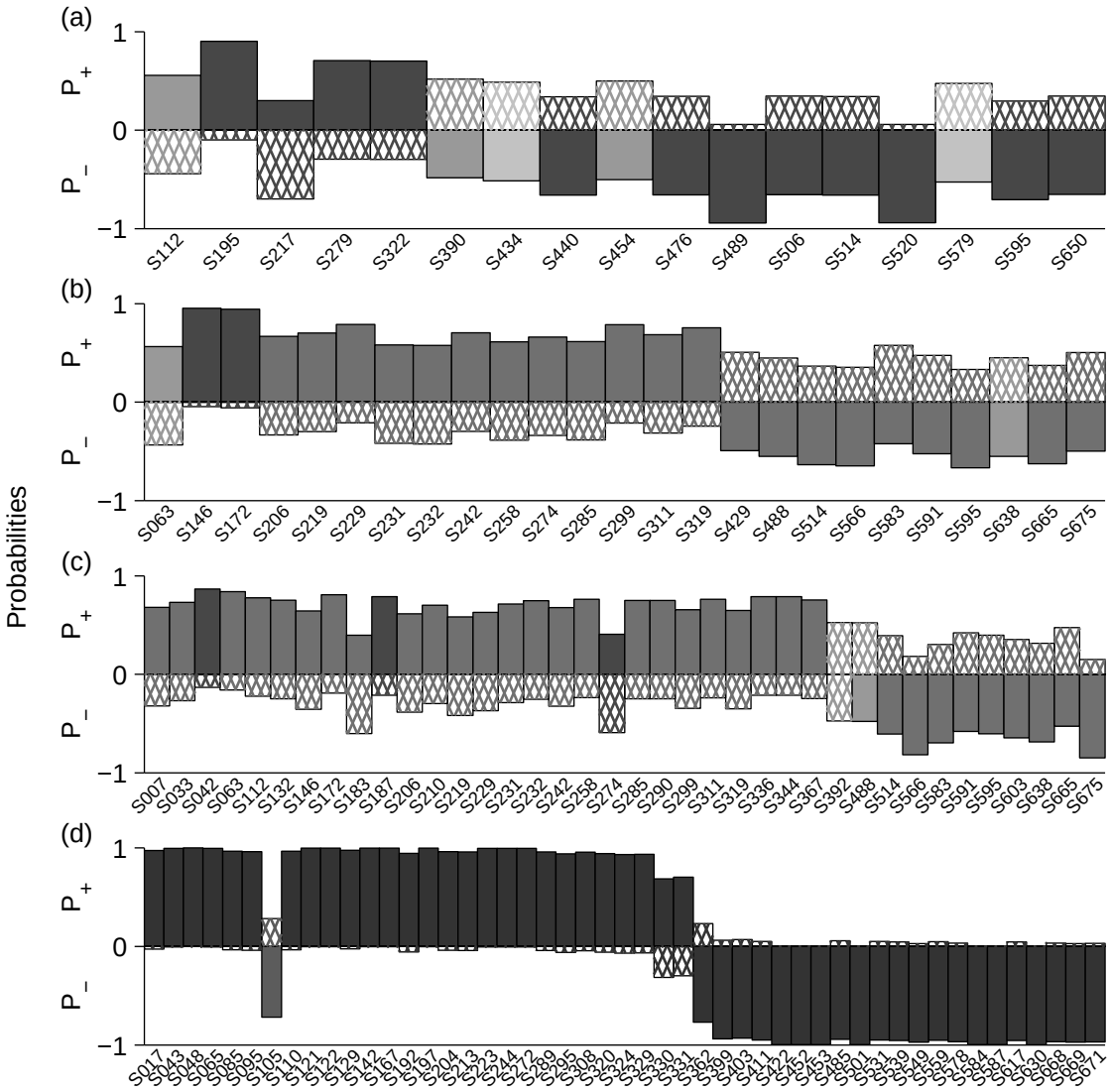

Figure 10. Polarity PDF plots (Fig. 7) with synthetic events for different numbers of stations and different noise environments. (a) has arrivals with a signal-to-noise ratio around 5, while (b) and (c) have arrivals with a signal-to-noise ratio of 7 and (d) has arrivals with a signal-to-noise ratio around 10.

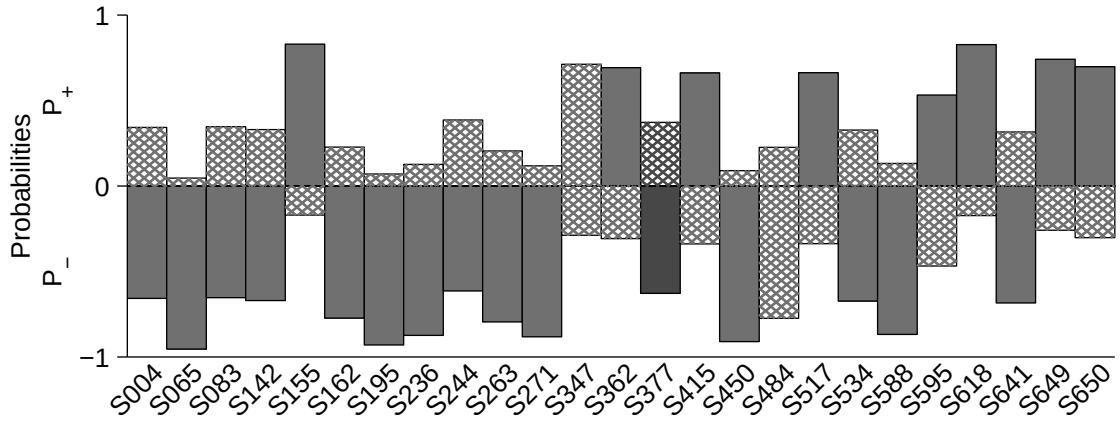

Figure 11. Polarity PDF plot (Fig. 7) of solutions from SH phase picking of a synthetic event with a signal-to-noise ratio of approximately 5.

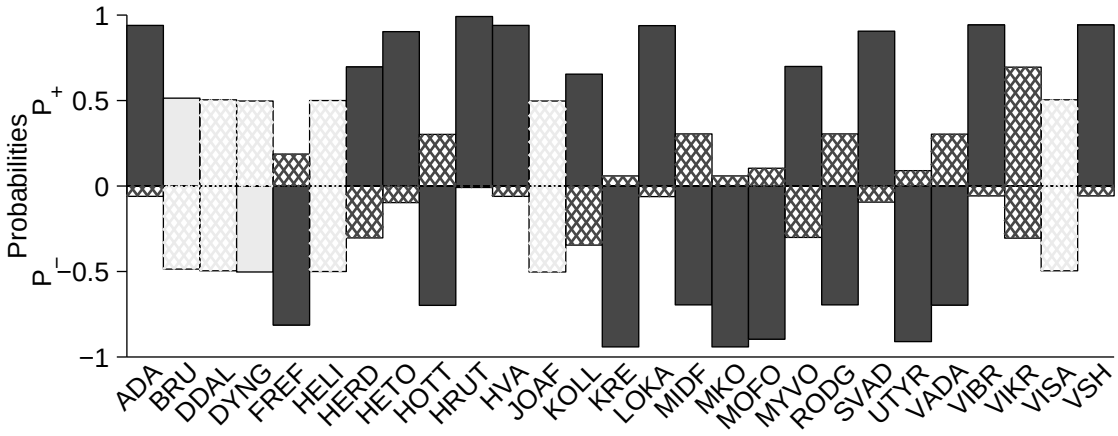

Figure 12. Polarity PDF plot (Fig. 7) for the 2007/07/06 20:47 event (White et al., 2011) shown in Table 1.

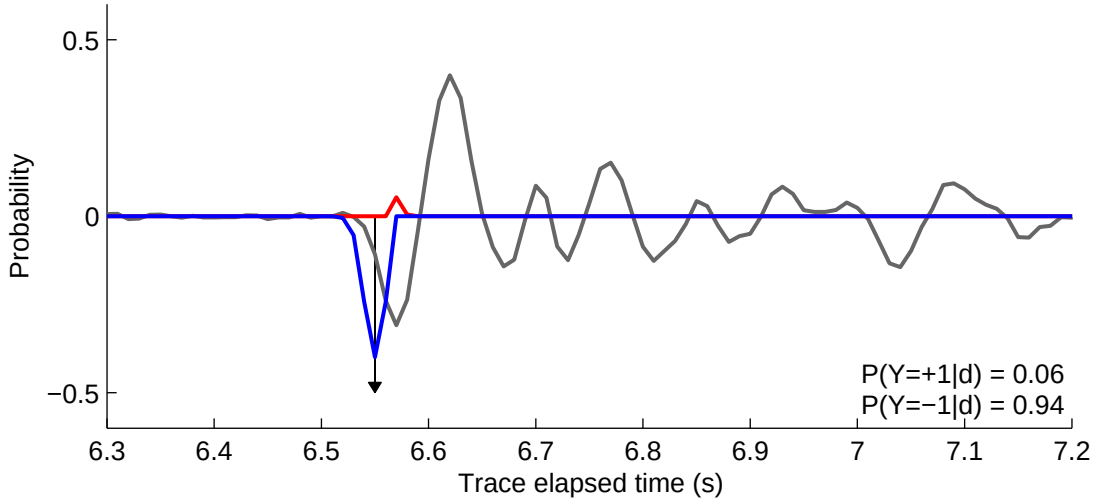

Figure 13. Example polarity PDFs and waveform from the 2007/07/06 20:47 event for station KRE. The positive polarity PDF is shown in red and the negative polarity PDF is shown in blue and as negative for clarity. The (scaled) waveform is in grey; the P-arrival-time pick and manual polarity pick are indicated by the arrow. The time-marginalised automated polarity probabilities are $\mathrm{p}\left(Y = +|\tau, \sigma_{\mathrm{mes}}, \sigma_\tau\right) = 0.06$ and $\mathrm{p}\left(Y = -|\tau, \sigma_{\mathrm{mes}}, \sigma_\tau\right) = 0.94$.

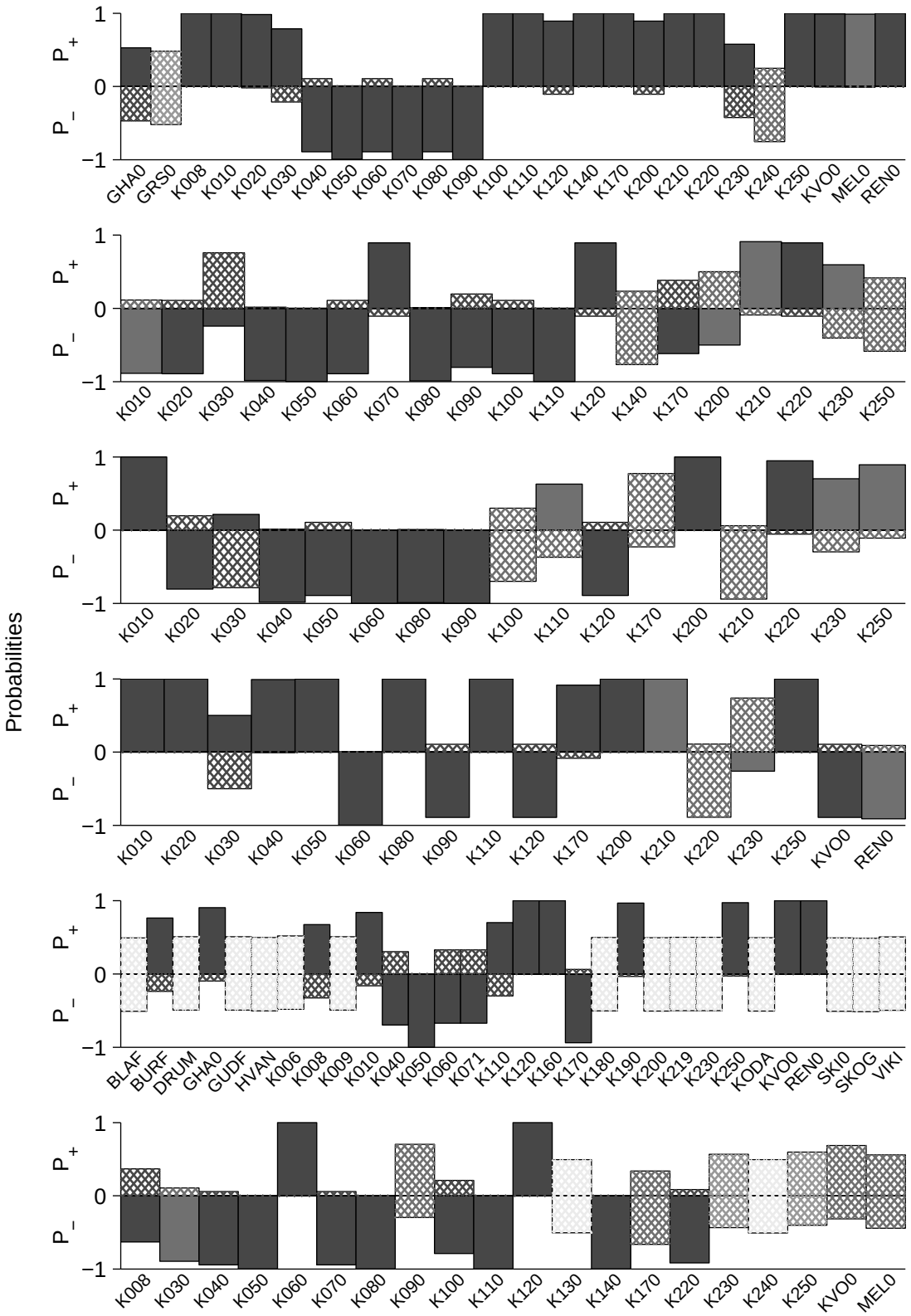

Figure 14. Polarity PDF plots (Fig. 7) for example events from the Krafla central volcano in the Northern Volcanic Zone of Iceland.

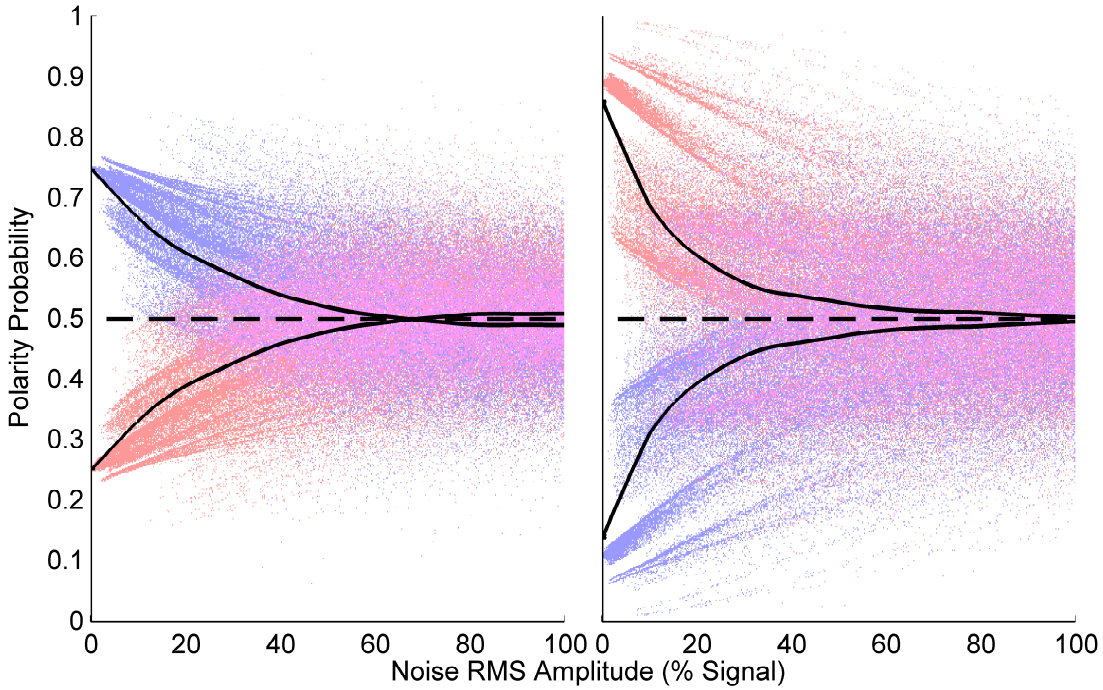

Figure 15. Distribution of the positive (red) and negative (blue) polarity probabilities for 100 000 samples of two real traces from Upptyppingar and Krafla, left and right columns, respectively, with added random Gaussian noise. The original waveform for the left plot had a negative polarity, and the right plot had a positive polarity. The arrival-time pick position was not changed, but the time uncertainty was increased as the noise level increased. The dashed line indicates a 50% probability of positive or negative arrival, corresponding to no net information, and the solid lines indicate a smoothed mean of the positive and negative polarity probabilities.

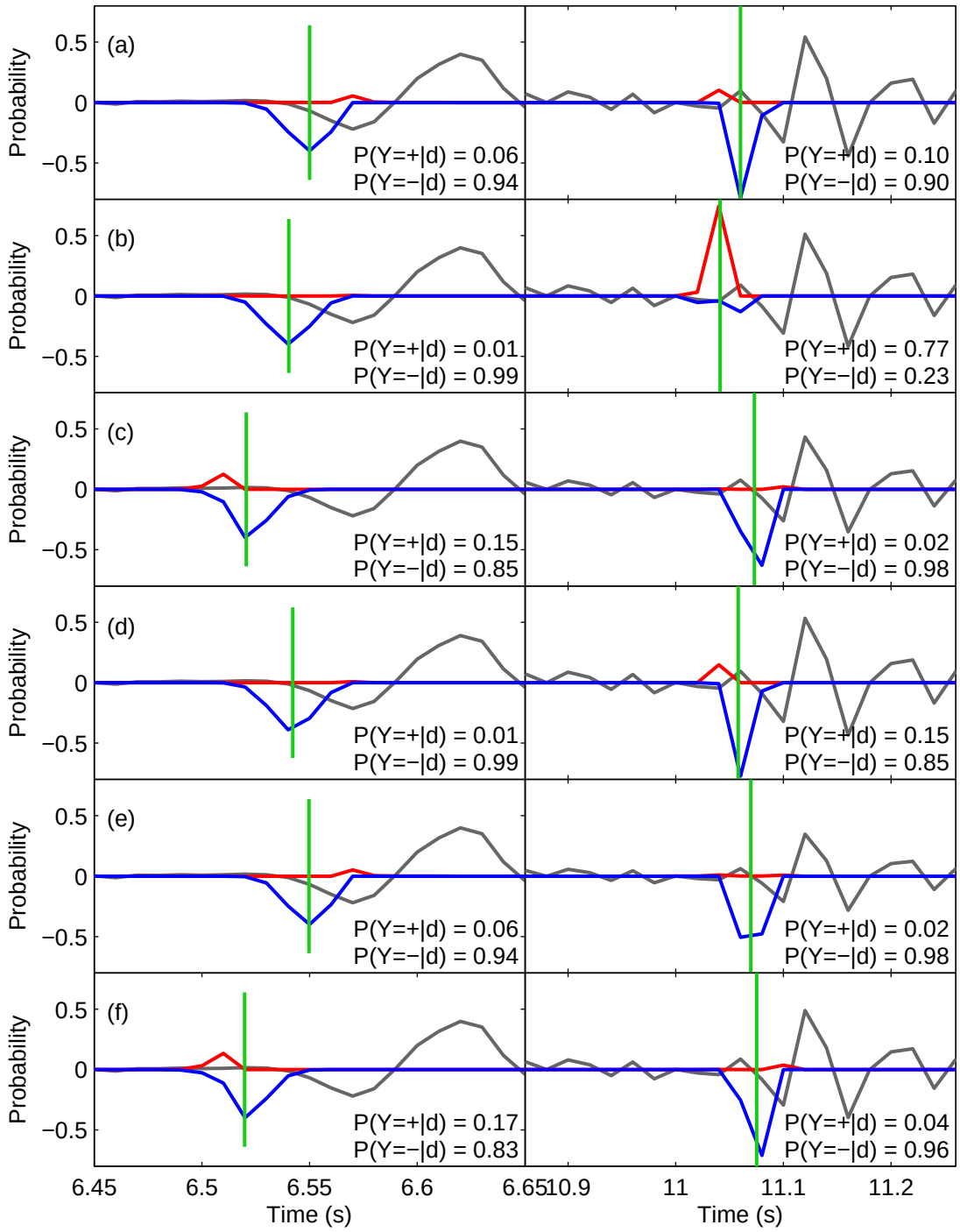

Figure 16. PDF plots for varying arrival-time picks for two real waveforms from Upptyppingar and Krafla, left and right columns, respectively. The original arrival-time pick is shown in (a), with randomly varied arrival-time picks in (b-f). The waveform is shown in grey, with the positive polarity PDF in red and the negative polarity PDF in blue. The vertical lines correspond to the arrival-time pick. The arrival-time picks were varied by adding a time shift randomly sampled from a Gaussian distribution.

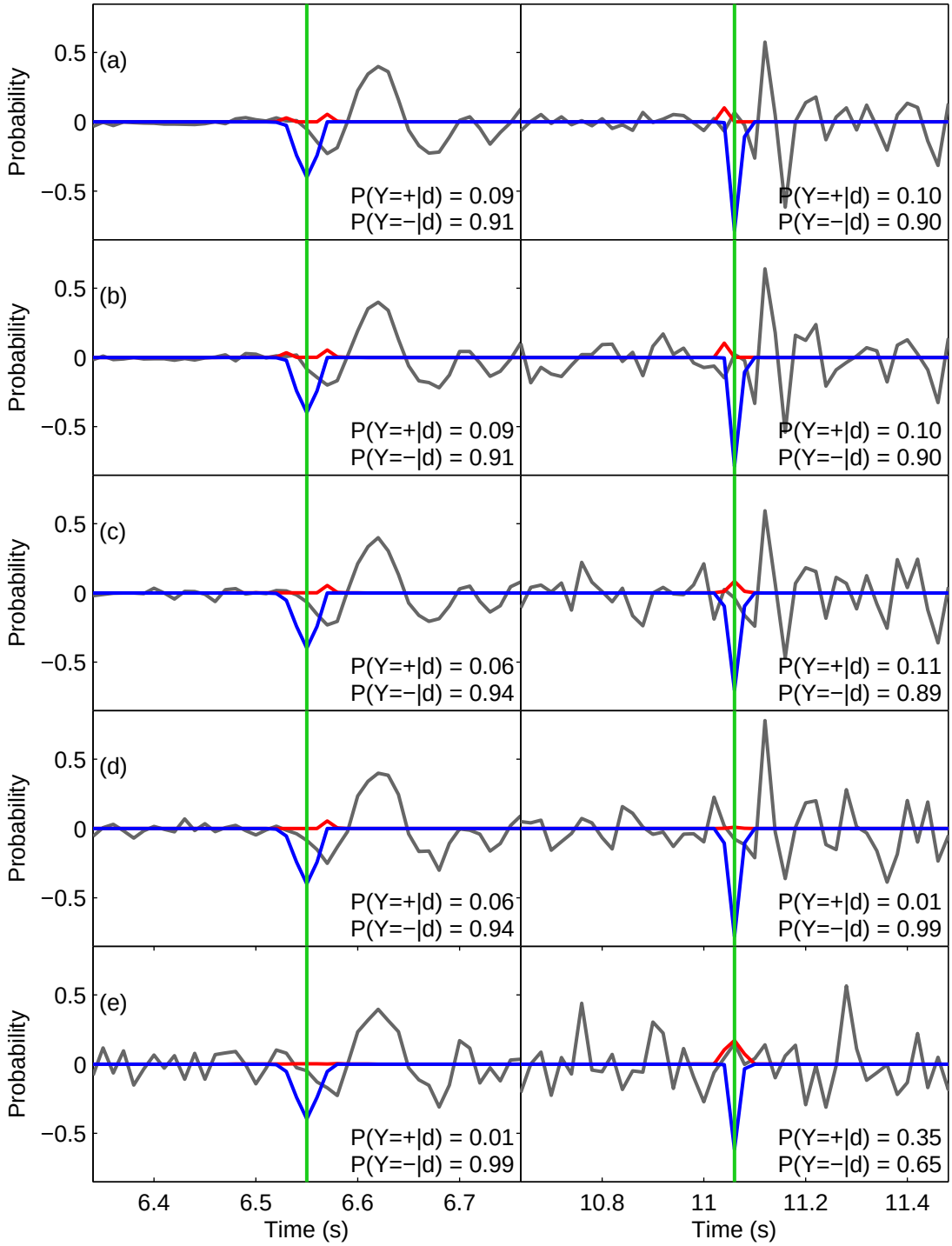

Figure 17. PDF plots for varying Gaussian noise levels on two real waveforms from Upptyppingar and Krafla, left and right columns, respectively. The noise levels are: (a) SNR=10, (b) SNR=5, (c) SNR=3, (d) SNR=2, and (e) SNR=1.2. The waveform is shown in grey, with the positive polarity PDF in red and the negative polarity PDF in blue. The vertical lines correspond to the arrival-time pick.

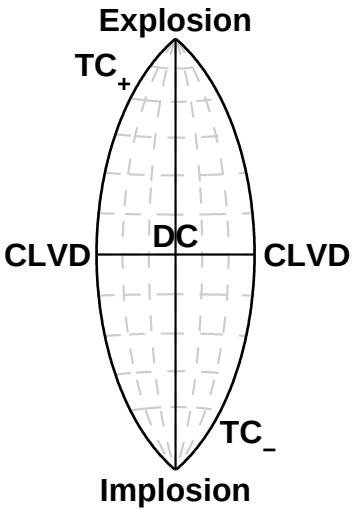

Figure 18. Example of the fundamental eigenvalue lune (Tape & Tape 2012), showing the position of the different source types. The horizontal axis corresponds to the eigenvalue longitude γ $\left(-\frac{\pi}{6} \leqslant \gamma \leqslant \frac{\pi}{6}\right)$ and the vertical axis, the eigenvalue latitude δ $\left(-\frac{\pi}{2} \leqslant \delta \leqslant \frac{\pi}{2}\right)$. The double-couple point (DC) lies at the intersection of the two lines. TC_+ and TC_- correspond to the opening and closing variants of the tensile crack model (Shimizu et al. 1987). The two compensated linear vector dipole (CLVD) sources (Knopoff & Randall 1970) are also shown on the plot.

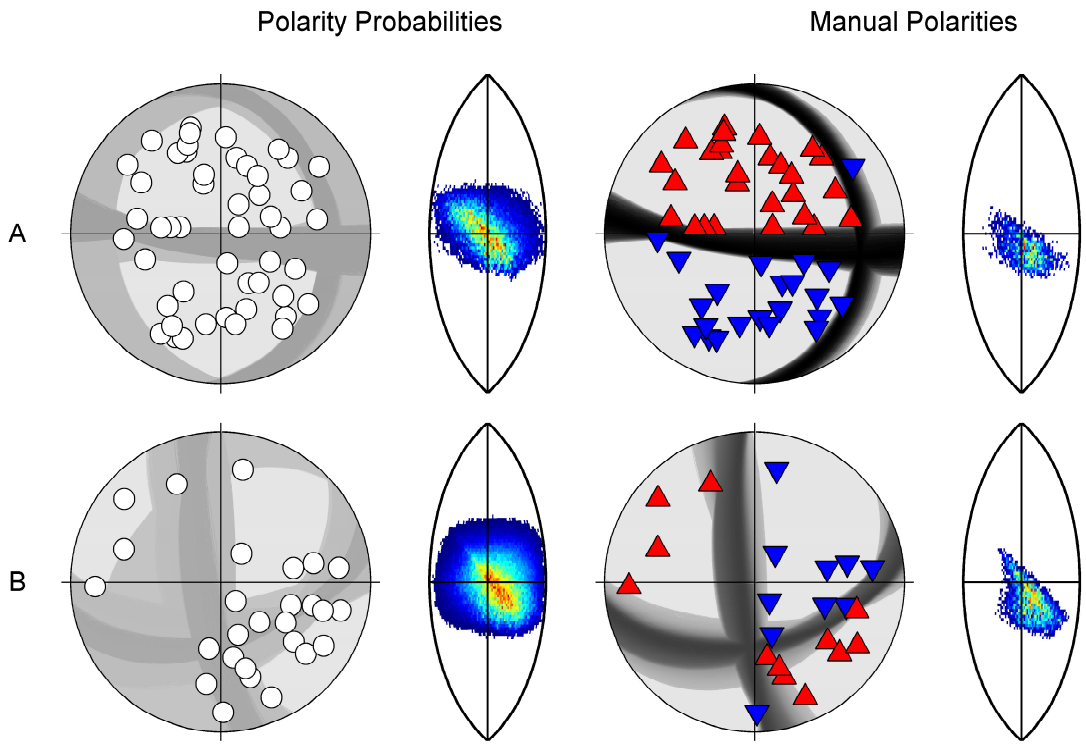

Figure 19. Comparison between automated polarity and manual polarity source inversions for two events, one synthetic (A) and the event from Table 1 and Fig. 12 (B). The first and second columns are the double-couple source PDFs for the automated polarity probabilities and manual polarity observations, respectively. The third and fourth columns are the full moment tensor PDFs for the automated polarity probabilities and manual polarity observations, respectively. The fault plane plots show the most likely solutions with the darkest lines. The stations are indicated by circles for the automated polarity probabilities, as no manual polarity information is used, and upwards red triangles or downwards blue triangles depending on the manually observed polarity. The lune plots are normalised and marginalised to show the most likely source type; red regions correspond to high probability and blue to low probability. Fig. 18 shows the positions of the different source types on the lune plot.

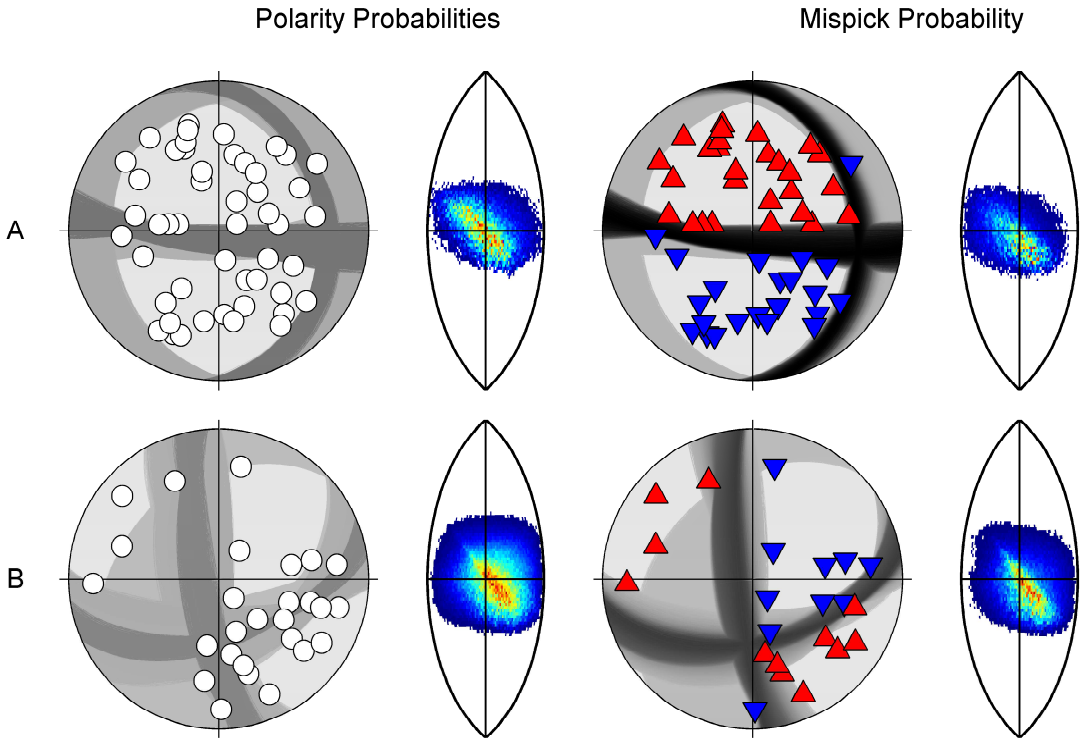

Figure 20. Comparison of automated polarity and arbitrary probability of a mistaken pick ($p_{\text{mispick}} = 0.1$) for two events, one synthetic (A) and the event from Table 1 and Fig. 12 (B). The first and second columns are the double-couple source PDFs for the automated polarity probabilities and manual polarity observations with mispick, respectively. The third and fourth columns are the full moment tensor PDFs for the automated polarity probabilities and manual polarity observations with mispick, respectively. The fault plane plots show the most likely solutions with the darkest lines. The stations are indicated by circles if there is no manual polarity information used, and upwards red triangles or downwards blue triangles depending on the manually observed polarity. The lune plots are normalised and marginalised to show the most likely source type; red regions correspond to high probability and blue to low probability. Fig. 18 shows the positions of the different source types on the lune plot.

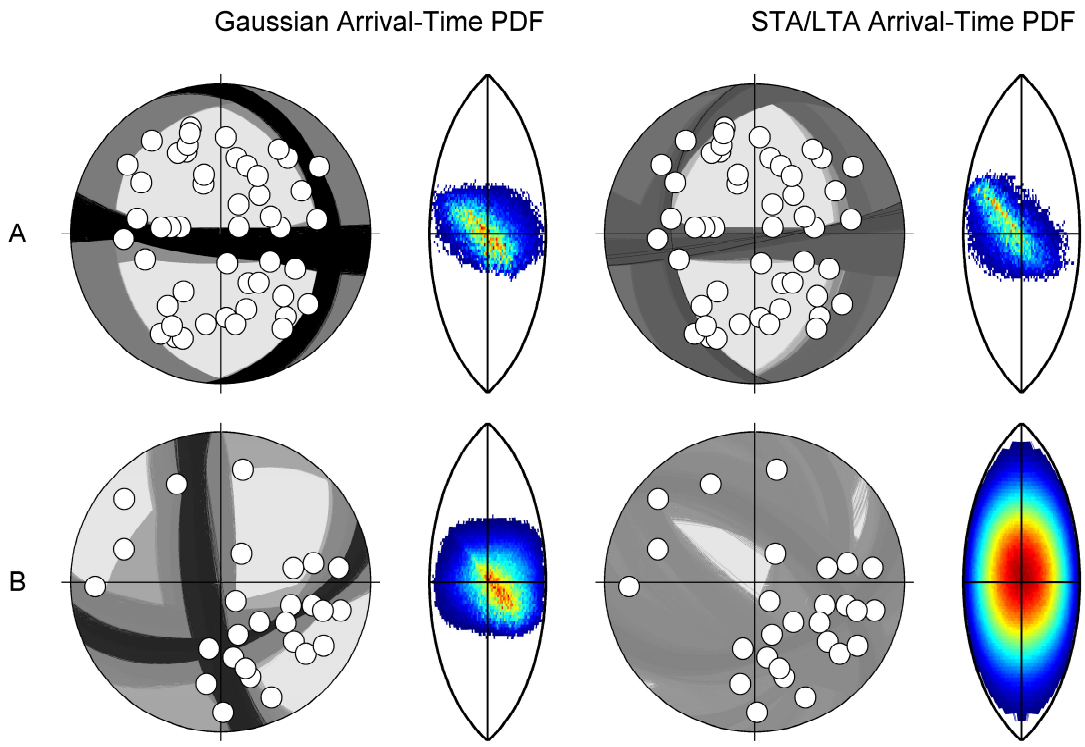

Figure 21. Comparison of automated polarity using a Gaussian time PDF around the manual time pick and STA/LTA time picking for two events, one synthetic (A) and the event from Table 1 and Fig. 12 (B). The first and second columns are the double-couple source PDFs for the Gaussian time PDF and the STA/LTA time PDF, respectively. The third and fourth columns are the full moment tensor PDFs for the Gaussian time PDF and the STA/LTA time PDF, respectively. The fault plane plots show the most likely solutions with the darkest lines. The stations are indicated by circles for the automated polarity probabilities, as no manual polarity information is used, and upwards red triangles or downwards blue triangles depending on the manually observed polarity. The lune plots are normalised and marginalised to show the most likely source type; red regions correspond to high probability and blue to low probability. Fig. 18 shows the positions of the different source types on the lune plot.

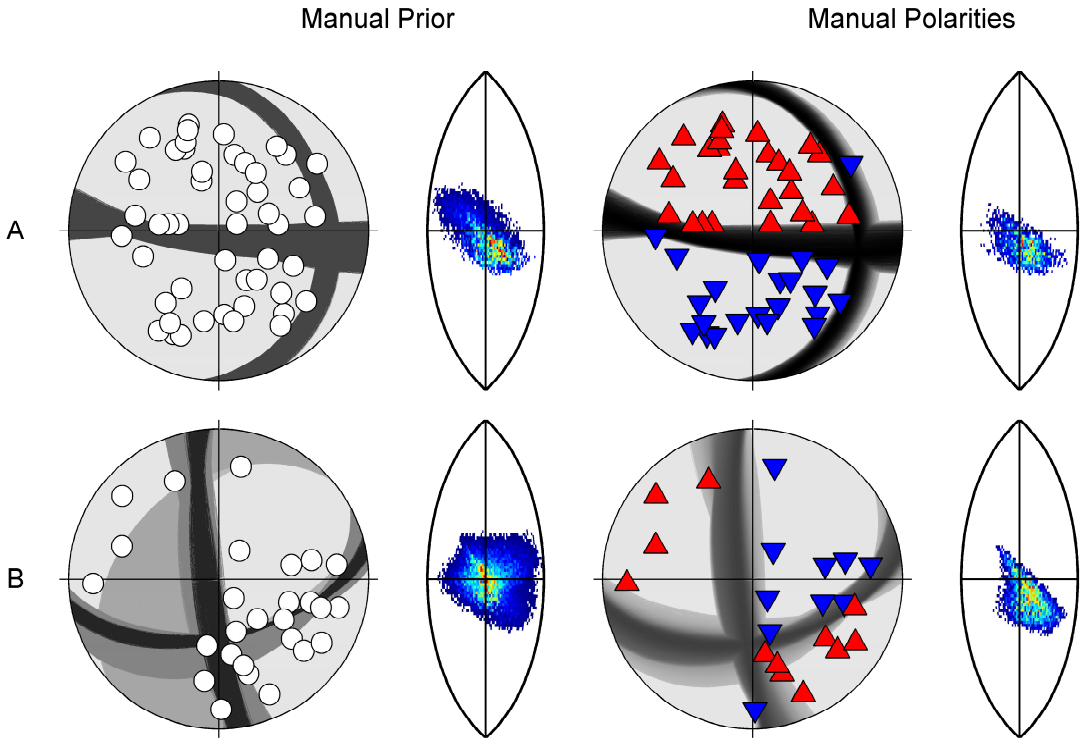

Figure 22. Comparison of automated polarity using a manual prior of 0.85 and manual polarity source inversions for two events, one synthetic (A) and the event from Table 1 and Fig. 12 (B). The first and second columns are the double-couple source PDFs for the automated polarity probabilities with a manual prior and manual polarity observations, respectively. The third and fourth columns are the full moment tensor PDFs for the automated polarity probabilities with a manual prior and manual polarity observations, respectively. The fault plane plots show the most likely solutions with the darkest lines. The stations are indicated by circles for the automated polarity probabilities, as no manual polarity information is used, and upwards red triangles or downwards blue triangles depending on the manually observed polarity. The lune plots are normalised and marginalised to show the most likely source type;red regions correspond to high probability and blue to low probability. Fig. 18 shows the positions of the different source types on the lune plot.

Station	Time Pick Quality	Manual Polarity	$\mathrm{p}(Y=+\|\tau,\sigma_{\mathrm{mes}},\sigma_\tau)$	$\mathrm{p}(Y=-\|\tau,\sigma_{\mathrm{mes}},\sigma_\tau)$
ADA	**Good**	+	**0.94**	0.06
BRU	Poor	+	0.51	0.49
DDAL	Poor		0.50	0.50
DYNG	Poor	–	0.50	0.50
FREF	**Good**	–	0.19	**0.81**
HELI	Poor		0.50	0.50
HERD	**Good**	+	**0.70**	0.30
HETO	**Good**	+	**0.90**	0.10
HOTT	**Good**	–	0.30	**0.70**
HRUT	**Good**	+	**0.99**	0.01
HVA	**Good**	+	**0.94**	0.06
JOAF	Poor		0.50	0.40
KOLL	**Good**	+	**0.65**	0.35
KRE	**Good**	–	0.06	**0.94**
LOKA	**Good**	+	**0.94**	0.06
MIDF	**Good**	–	0.30	**0.70**
MKO	**Good**	–	0.06	**0.94**
MOFO	**Good**	–	0.10	**0.90**
MYVO	**Good**	+	**0.70**	0.30
RODG	**Good**	–	0.30	**0.70**
SVAD	**Good**	+	**0.90**	0.10
UTYR	**Good**	–	0.09	**0.91**
VADA	**Good**	–	0.30	**0.70**
VIBR	**Good**	+	**0.94**	0.06
VIKR	Good		0.69	0.31
VISA	Poor		0.50	0.50
VSH	**Good**	+	**0.94**	0.06

Table 1. Comparison of automated and manual polarity picks for the 2007/7/6 20:47 Upptyppingar event (White et al. 2011). Missing manual polarities are unpicked. Time pick qualities are manually assigned as good or poor with associated time pick errors of 0.01 s and 0.5 s. These qualities would correspond to 0 and 3 from the HYPO71 pick weighting (Lee & Lahr 1975). pPositive is the probability of a positive polarity and pNegative the probability of a negative polarity. The bolded probabilities correspond to values larger than 0.6 which agree with the manual polarity pick for good (pick quality 0) picks.